nature structural & molecular biology

Article

https://doi.org/10.1038/s41594-025-01533-5

piRNA gene density and SUMOylation organize piRNA transcriptional condensate formation

Received: 5 December 2023

Accepted: 12 March 2025

Published online: 02 May 2025

Check for updates

Chengming Zhu[1,2,5], Xiaoyue Si[1,5], Xinhao Hou[1], Panpan Xu[1], Jianing Gao[1], Yao Tang[1], Chenchun Weng[1], Mingjing Xu[1], Qi Yan[1], Qile Jin[1], Jiewei Cheng[1], Ke Ruan[1], Ying Zhou[1], Ge Shan[1], Demin Xu[1], Xiangyang Chen[1], Shengqi Xiang[1] ✉, Xinya Huang[1] ✉, Xuezhu Feng[3] ✉ & Shouhong Guang[1,4] ✉

Piwi-interacting RNAs (piRNAs) are essential for maintaining genome integrity and fertility in various organisms. In flies and nematodes, piRNA genes are encoded in heterochromatinized genomic clusters. The molecular mechanisms of piRNA transcription remain intriguing. Through small RNA sequencing and chromatin editing, we discovered that spatial aggregation of piRNA genes enhances their transcription in nematodes. The facultative heterochromatinized piRNA genome recruits the piRNA upstream sequence transcription complex (USTC; including PRDE-1, SNPC4, TOFU-4 and TOFU-5) and the H3K27me3 reader UAD-2, which phase-separate into droplets to initiate piRNA transcription. We searched for factors that regulate piRNA transcription and isolated the SUMO E3 ligase GEI-17 as inhibiting and the SUMO protease TOFU-3 as promoting piRNA transcription foci formation, thereby regulating piRNA production. Our study revealed that spatial aggregation of piRNA genes, phase separation and deSUMOylation may benefit the organization of functional biomolecular condensates to direct piRNA transcription in the facultative heterochromatinized genome.

Piwi-interacting RNAs (piRNAs) belong to a class of small noncoding RNAs that form complexes with Piwi proteins to repress transposable elements and regulate gene expression[1–9]. In *Caenorhabditis elegans*, piRNAs originate from two large genomic clusters located on chromosome IV (refs. 10–12). These piRNA clusters are enriched with the repressive histone mark H3K27me3 (ref. 13). piRNAs are independently transcribed as short capped transcripts by RNA polymerase II, generating piRNA precursor transcripts[10–12]. The upstream sequence transcription complex (USTC), which is essential for piRNA transcription, is enriched on the upstream Ruby motif of type I piRNAs and promotes piRNA precursor transcription[14]. The USTC complex consists of four proteins: PRDE-1, SNPC4, TOFU-4 and TOFU-5 (refs. 10,14,15). These proteins generate distinct subnuclear foci that colocalize with piRNA clusters in the nucleus[14]. The chromodomain protein UAD-2 recognizes the histone mark H3K27me3 and facilitates the recruitment of the USTC complex to piRNA genes[16]. Recent studies have shown that

[1]Department of Obstetrics and Gynecology, The First Affiliated Hospital of USTC, The USTC RNA Institute, Ministry of Education Key Laboratory for Membraneless Organelles & Cellular Dynamics, Hefei National Research Center for Physical Sciences at the Microscale, Center for Advanced Interdisciplinary Science and Biomedicine of IHM, School of Life Sciences, Division of Life Sciences and Medicine, University of Science and Technology of China, Hefei, China. [2]School of Life Sciences, Anhui Medical University, Hefei, China. [3]School of Basic Medical Sciences, Anhui Medical University, Hefei, China. [4]CAS Center for Excellence in Molecular Cell Science, Chinese Academy of Sciences, Hefei, China. [5]These authors contributed equally: Chengming Zhu, Xiaoyue Si. ✉e-mail: cqxiang@ustc.edu.cn; hxy1996@ustc.edu.cn; fengxuezhu@ahmu.edu.cn; sguang@ustc.edu.cn

the localization of USTC to piRNA domains maintains high nucleosome density across piRNA clusters and the transcription of piRNA precursors and that casein kinase II-mediated phosphorylation of the USTC component TOFU-4 is also crucial for piRNA expression[17,18]. However, despite our knowledge of piRNA clusters and heterochromatic states being crucial for piRNA transcription, the mechanisms remain mysterious[13,16,19–23]. The underlying mechanisms of USTC assembly at piRNA loci and the activation of transcription in H3K27me3 domains are yet to be fully understood[18].

In *Drosophila* ovarian germ cells, piRNAs are produced from dual-strand clusters embedded in heterochromatin marked by H3K9me3. The Rhino–Deadlock–Cutoff complex binds to heterochromatin and licenses noncanonical transcription of dual-strand piRNA clusters. Rhino's chromodomain recognizes H3K9me3 (refs. 24–26). *Drosophila* ovarian somatic cells also possess unistrand piRNA clusters that depend on the Nxf1–Nxt1 complex for nuclear export of spliced piRNA precursors[22,27]. However, it remains unclear how piRNA genes evolved into specialized genomic clusters and how heterochromatin readers such as Rhino and UAD-2 interface with the core transcriptional machinery[16,26].

In eukaryotes, biomolecular condensates form through liquid–liquid phase separation (LLPS) and have crucial roles in various processes[28–34]. Recent studies have revealed that the phase separation of transcription factors can mediate the formation of transcriptional hubs[35–37] and condensation of activators and cofactors into phase-separated compartments potentiates gene expression[38–41]. Hence, understanding whether and how phase separation underpins the compartmentalization of the heterochromatinized piRNA genome and transcriptional machinery will provide vital insights into the mechanism of gene regulation.

Small ubiquitin-like modifier (SUMO) is an essential posttranslational modification that regulates diverse cellular processes, including transcription, DNA repair, RNA processing, ribosome biogenesis, cell-cycle control and nuclear body formation[42,43]. Moreover, SUMOylation orchestrates the activity of transcription factors and phase separation of chromatin modifiers to control gene expression programs[44–46]. SUMOylation of piRNA pathway proteins provides a molecular switch to connect piRNA target recognition to downstream chromatin silencing machinery, enabling heterochromatin formation and transcriptional silencing of piRNA target genes[47–51]. Defining the mechanisms of SUMOylation-mediated control of piRNA transcription condensate formation will provide critical insights into the molecular underpinnings of piRNA production and genome regulation.

In this work, we show that the spatial clustering of piRNA genes into dense genomic loci promotes piRNA transcription in *C. elegans* through phase separation of piRNA transcription factors into condensates at piRNA clusters. The regulated SUMOylation serves as a critical determinant directing USTC and UAD-2 condensation and piRNA synthesis. Our findings present a mechanistic model wherein piRNA gene clustering density, UAD-2 phase separation properties and SUMOylation status collaboratively assemble functional piRNA transcription compartments.

Results

Clustered piRNA genes promote piRNA expression in nematodes

The *C. elegans* genome contains approximately 15,000 annotated piRNA genes distributed across six chromosomes, with ~92% located within the two major piRNA clusters on chromosome IV (Extended Data Fig. 1a)[11]. piRNA cluster I is a 2.5-Mb region on the center of chromosome IV, containing ~200 piRNA genes per 100 kb. piRNA cluster II is a 3.7-Mb region on the right arm of chromosome IV, containing ~400 piRNA genes per 100 kb (Fig. 1a)[13,52]. In the meiotic zone, we can observe only one piRNA transcription focus per nucleus (Fig. 1b,c). To determine which part of the piRNA genome corresponds to the USTC and UAD-2 foci, we designed a lacI::tagRFP–lacO labeling system to display piRNA cluster II (Extended Data Fig. 1b,c). We generated an *rps-2p*::lacI::tagRFP transgene (Extended Data Fig. 1b), where lacI::tagRFP is expressed in the meiotic zone of the gonad (Extended Data Fig. 1d,e). We subsequently introduced a 256× lacO sequence into the middle of the cluster II at linkage group (LG) IV position 15,809,942 (contributed by the C. Frøkjær-Jensen lab) in the lacI::tagRFP strain (Extended Data Fig. 1c). We observed that the UAD-2 and TOFU-4 foci colocalized with lacI::tagRFP, suggesting that the USTC components and UAD-2 may primarily accumulate on the piRNA cluster II region (Extended Data Fig. 1d–g). To further validate this conclusion, we used the SYP1 protein of the synaptonemal complex as a marker to label the chromosomes in pachytene cells of the gonad[53]. Through fluorescence imaging, we observed that the H3K27me3 reader UAD-2 and the piRNA transcription factor TOFU-4 form a single nuclear focus concentrated on chromosome IV, corresponding to the cluster II genome, in the nucleus of each pachytene germ cell (Fig. 1b,c)[14,16]. In contrast, cluster I and out-cluster regions exhibited minimal, if detectable, GFP foci.

In *C. elegans*, piRNA expression shows distinct sex specificity, with notable differences during oogenesis and spermatogenesis[54,55]. We also observed that UAD-2, PRDE-1, TOFU-4 and TOFU-5 each form a distinct piRNA focus per nucleus in the spermatogenesis region of L4-stage hermaphrodites (Extended Data Fig. 1h–k). During spermatogenesis in the male germline, UAD-2 and USTC also form piRNA foci, with only one prominent focus per nucleus in the meiotic zone (Extended Data Fig. 1l–o).

piRNA genes have been previously classified into type I and type II according to the presence of a Ruby motif in the promoter sequence[11,13,52]. We analyzed the chromatin immunoprecipitation sequencing (ChIP-seq) data and found that UAD-2, TOFU-4 and TOFU-5 exhibit binding capabilities to both type I and type II piRNA genes, yet with a much lower affinity to type II piRNAs (Extended Data Fig. 2a–c). To investigate the binding affinity of UAD-2 and USTC to different clusters, we categorized the data by clusters and quantified the binding intensity of UAD-2, TOFU-4 and TOFU-5 accordingly. Our data revealed enriched binding of UAD-2 and the USTC components (TOFU-4 and TOFU-5) on the cluster II genome compared to cluster I and out-cluster regions (Fig. 1d).

To characterize piRNA expression, we analyzed the piRNA population from total small RNAs or PRG1-associated small RNAs in wild-type adult animals (Extended Data Fig. 2d). The expression pattern of piRNAs across chromosome IV based on total small RNA and PRG1-immunoprecipitated small RNA displayed enriched expression in the two clusters (Fig. 1e,f). piRNAs in cluster II showed substantially higher expression levels than those in cluster I and out-cluster regions. Specifically, cluster II piRNAs exhibited an average expression of approximately 14.2 reads per million (RPM) in the total RNA sequencing (RNA-seq) and ~80.2 RPM in PRG1-associated RNA-seq. In contrast, cluster I piRNAs exhibited lower expression, while out-cluster piRNAs displayed further reduced expression (Fig. 1g,h). Among all piRNA genes, the cluster I and out-cluster genomes contained 18% and 8%, respectively, of the total number of piRNA genes and expressed a minor fraction of piRNA reads (Fig. 1i). In comparison, cluster II contained 74% of piRNA genes and expresses close to 92% (total RNA) and 94% (PRG1-associated RNA) of piRNA reads (Fig. 1i).

To further test whether the clustering of piRNA genes is important for piRNA expression, we analyzed the distribution and expression of piRNAs in another nematode, *C. briggsae*. The *C. briggsae* genome contains over 25,000 piRNAs across six chromosomes[56], clustering into one locus on LG I and two loci on LG IV, which are termed clusters 1, 2 and 3, respectively (Extended Data Fig. 2e). The published *C. briggsae* piRNA high-throughput sequencing data[56] showed that, similarly to *C. elegans*, piRNA genes located within clusters exhibited explicitly higher expression compared to those of out-cluster regions. The average expression level of clustered piRNAs bound to the Piwi protein

https://doi.org/10.1038/s41594-025-01533-5

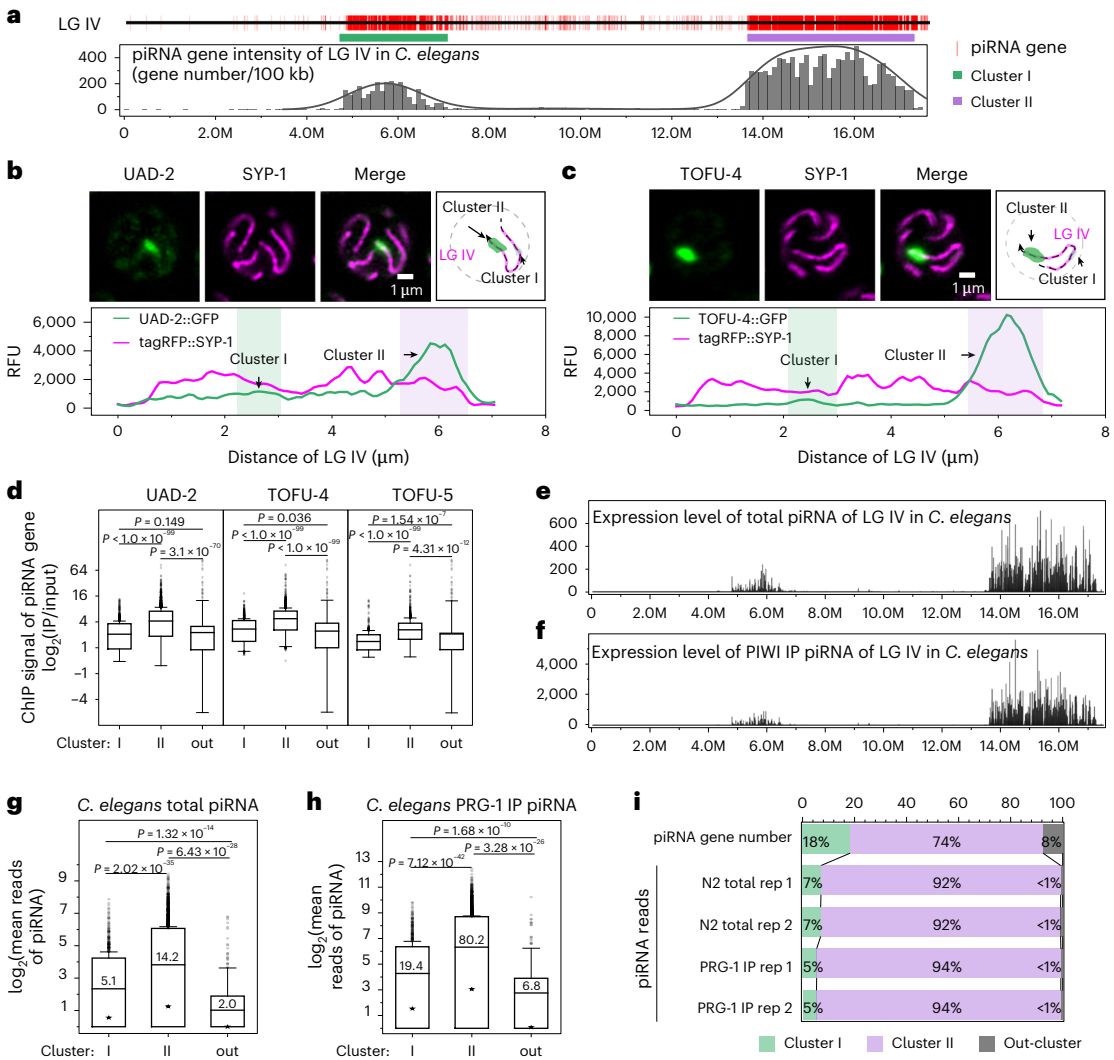

Fig. 1 | Clustered piRNA genes promote piRNA expression in *C. elegans*. **a**, Top: the localization of piRNA genes (marked in red) on *C. elegans* chromosome IV. The green and purple segments indicate cluster I and cluster II loci, respectively. Bottom: the piRNA gene density on chromosome IV, representing the number of piRNA genes per 100-kb segment. **b**, Top: the localization of UAD-2::GFP and tagRFP::SYP1. Bottom: the relative fluorescence unit intensity (RFU) of UAD-2 and SYP1 along chromosome IV, marked by a dashed line. All images were taken by the Leica Thunder imaging system and deconvoluted using Leica Application Suite X software (version 3.7.4.23463). All images are representative of more than three animals. **c**, Top: the localization of TOFU-4::GFP and tagRFP::SYP1. Bottom: the RFU of TOFU-4 and SYP1 along chromosome IV, marked by a dashed line. **d**, Box plots revealing the ChIP signal (log_2(IP/input)) of piRNA genes for the indicated protein from one biological replicate. The box itself represented the interquartile range between 10% and 90%, thereby encompassing the middle 80% of the dataset. The central horizontal line within the box represents the mean value. Error bars represent the mean ± 1.5 s.d., indicating the variability of the data around the mean. Outliers are individually marked as points, representing data points that fall outside the range of the mean ± 1.5 s.d. A two-tailed *t*-test was performed to determine statistical significance. **e**, Graphs presenting the expression levels of total piRNAs from LG IV based on average reads from two biological replicates, normalized as RPM + 1. **f**, Graphs presenting the expression levels of PRG1-associated piRNAs from LG IV based on average reads from two biological replicates, normalized as RPM + 1. In **a**, **e** and **f**, the *x* axis unit is base pairs (bp), where 'M' denotes million. **g**, Box plots revealing log_2(average piRNA reads of two biological replicates) for total piRNA across cluster I, cluster II and out-cluster regions, normalized as RPM + 1. The box itself represents the interquartile range between 5% and 95%, thereby encompassing the middle 90% of the dataset. The central horizontal line and the adjacent numeric value within the box represent the mean value. The star within the box represents the median value. Error bars represent the mean ± 1.5 s.d., indicating the variability of the data around the mean. Outliers are individually marked as points, representing data points that fall outside the range of mean ± 1.5 s.d. Statistical significance was determined using a two-sample *t*-test. **h**, Box plots revealing log_2(average piRNA reads of two biological replicates) for PRG1-associated piRNAs across cluster I, cluster II and out-cluster regions, normalized as RPM + 1. Statistical significance was determined using a two-sample *t*-test. **i**, Graphs presenting the fractional distribution of piRNA genes and their corresponding expression reads of two biological replicates (normalized as RPM) across cluster I, cluster II and out-cluster loci.

was ~50 RPM, while out-cluster piRNAs showed an average of ~3.1 RPM (Extended Data Fig. 2f). Further analysis revealed that 32% of piRNA genes were encoded in out-cluster regions while generating only 2% of the total piRNA reads. In contrast, 68% of the piRNA genes were clustered and contributed 98% of the total piRNA reads (Extended Data Fig. 2g). In *C. briggsae*, the localization of piRNA genes within piRNA clusters is strongly correlated with their expression levels.

Interestingly, a recent study described a piRNA-mediated RNA interference (RNAi) system operating through an extrachromosomal array in *C. elegans*[57], in which a short genomic region (1.5 kb) that contained at least six highly expressed piRNAs and were repeated approximately 100 times in extrachromosomal arrays could promote efficient piRNA transcription. Notably, the piRNA density in these extrachromosomal arrays amounts to approximately 400 piRNAs per 100 kb, closely

https://doi.org/10.1038/s41594-025-01533-5

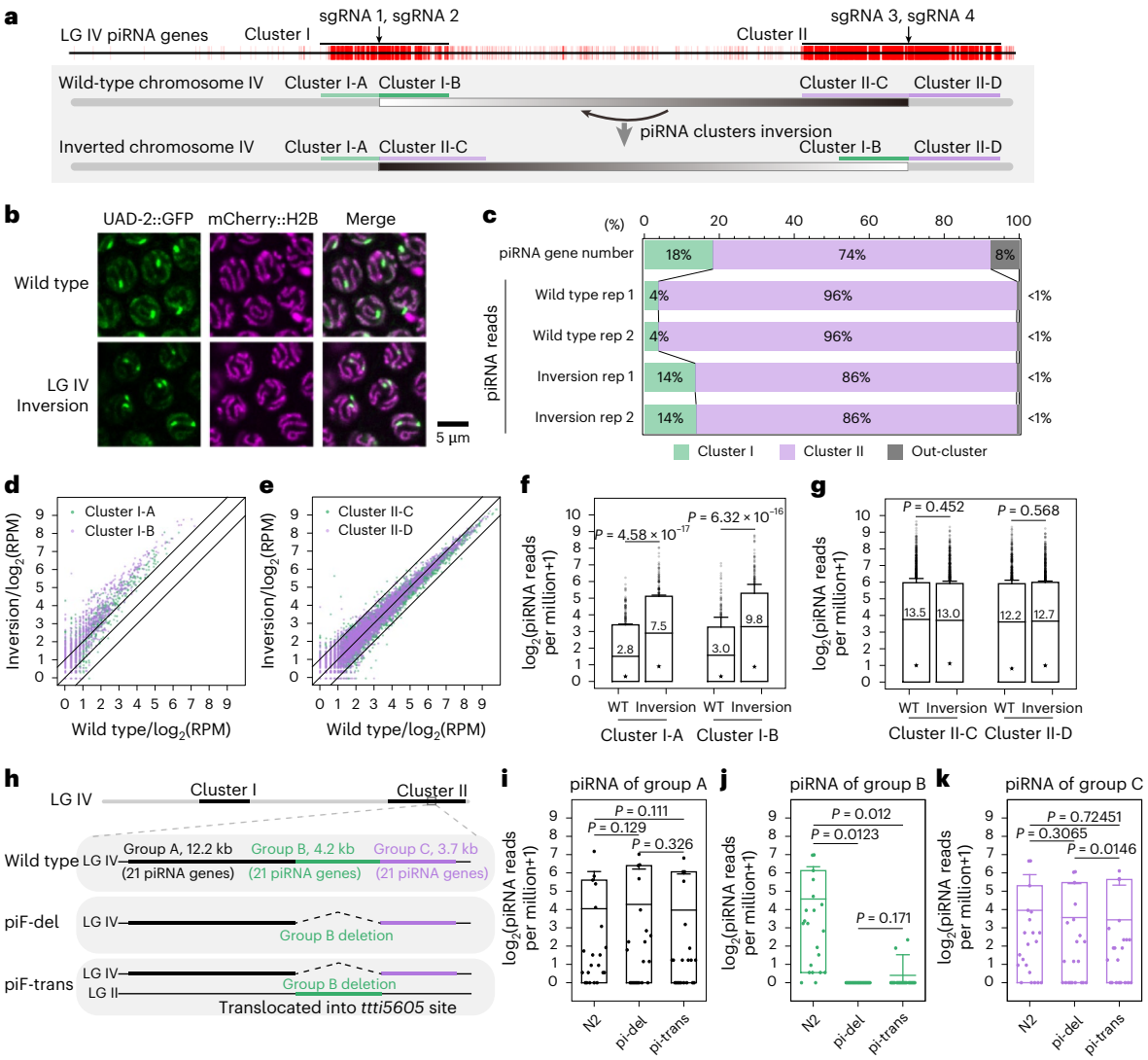

Fig. 2 | Chromosomal editing alters piRNA clustering and expression. **a**, Schematic diagram displaying the CRISPR-mediated intrachromosomal inversion process. sgRNA1 and sgRNA2 target the center of cluster I, while sgRNA3 and sgRNA4 target the center of cluster II. Bottom: the inverted LG IV chromosome of the worm. **b**, Images showing the subcellular localization of UAD-2::GFP and mCherry::H2B in the nuclei of pachytene germ cells. In wild-type cells, a single UAD-2 bright spot is observed in each nucleus, whereas the inverted strain reveals two UAD-2 bright spots per nucleus. All images were taken by the Leica Thunder imaging system and deconvoluted using Leica Application Suite X software (version 3.7.4.23463). All images are representative of more than three animals. **c**, Graphs presenting the fractional distribution of piRNA genes and their corresponding expression reads of two biological replicates (normalized as RPM) for the indicated strains across cluster I, cluster II and out-cluster loci. **d**, Expression levels of piRNAs from cluster I between wild-type and inverted strains, presented using both box plots. All expression values are the average of two biological replicates and are normalized as RPM + 1. The box itself represents the interquartile range between 5% and 95%, thereby encompassing the middle 90% of the dataset. The central horizontal line and the adjacent numeric value within the box represent the mean value. The star within the box represents the median value. Error bars represent the mean ± 1.5 s.d., indicating the variability of the data around the mean. Outliers are individually marked as points, representing data points that fall outside the range of mean ± 1.5 s.d. Gray solid lines indicate reference slopes of $y = 2x$ (left), $y = x$ (center), and $y = 0.5x$ (right). Statistical significance was determined using a paired-sample *t*-test. **e**, Expression levels of piRNAs from cluster II between wild-type and inverted strains, presented using both box plots. **f**, Expression levels of piRNAs from cluster I between wild-type and inverted strains, presented using scatter plots. **g**, Expression levels of piRNAs from cluster II between wild-type and inverted strains, presented using scatter plots. **h**, Schematic diagram showing the CRISPR-mediated chromosomal translocation experiments. Group B piRNAs are translocated from cluster II of LG IV to the *ttti5605* site of LG II. **i**–**k**, Box plots revealing $\log_2$(normalized piRNA reads + 1) for the wild type, piRNA fragment deletion (piF-del) strain and piRNA fragment translocation (piF-trans) strain across groups A (**i**), B (**j**) and C (**k**) from a single biological replicate. The box itself represents the interquartile range between 10% and 90%, thereby encompassing the middle 80% of the dataset. The central horizontal line within the box represents the mean value. Error bars represent the mean ± 1.5 s.d., indicating the variability of the data around the mean. Outliers are individually marked as points, representing data points that fall outside the range of mean ± 1.5 s.d. Statistical significance was determined using a paired-sample *t*-test.

paralleling that observed in cluster II of *C. elegans*, further hinting that there may be a correlation between the gene density of piRNA genes on extrachromosomal arrays and their effective expression in *C. elegans*.

Thus, these data suggested that the clustering of piRNA genes into dense genomic regions may be critical for robust piRNA expression in both *C. elegans* and *C. briggsae*.

Intrachromosomal inversion alters piRNA expression

To test whether piRNA expression levels rely on gene density rather than their positions on chromosomes, we designed dual single guide RNA (sgRNA)-guided CRISPR–Cas9 technology to introduce chromosome inversion on LG IV (ref. 58). We designed four sgRNAs targeting the middle of cluster I and cluster II to cleave LG IV and screened for

https://doi.org/10.1038/s41594-025-01533-5

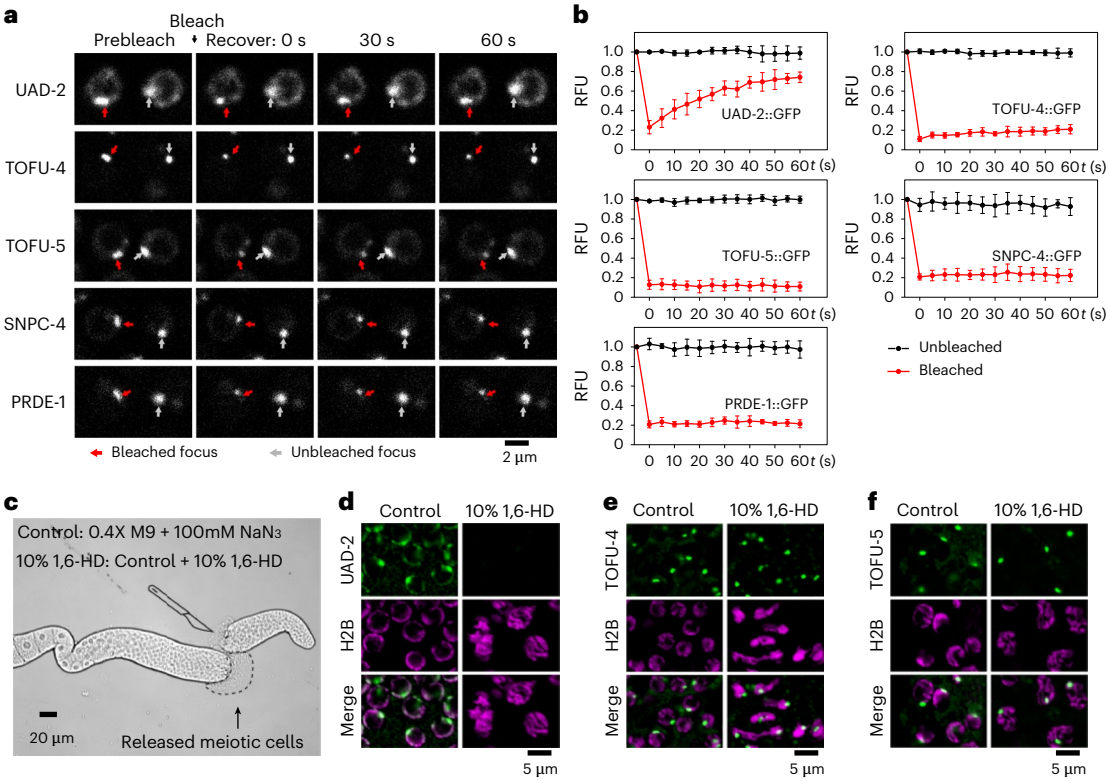

Fig. 3 | UAD-2 forms a liquid droplet-like condensate at piRNA cluster loci. **a**, FRAP of UAD-2::GFP and GFP-tagged USTC components (TOFU-4, TOFU-5, SNPC4 and PRDE-1) was conducted using a Zeiss LSM980 confocal microscope. All images are representative of six animals. **b**, Graphs presenting the RFU of the control area and bleached area of UAD-2 and the USTC components. Quantification of FRAP data from $n = 6$ independent animals, presented as the mean ± s.d. **c**, Images showing germline nuclei expressing UAD-2::GFP, TOFU-4::GFP or TOFU-5::GFP. After release by needle disruption, the germline was imaged within 5 min. Germlines were treated with 10% 1,6-HD to prohibit phase separation. All images were taken by the Leica Thunder imaging system and deconvoluted using Leica Application Suite X software (version 3.7.4.23463). All images are representative of more than three animals. **d**–**f**, Images showing germline nuclei expressing UAD-2::GFP (**d**), TOFU-4::GFP (**e**) and TOFU-5::GFP (**f**) under indicated experimental conditions.

lines with intrachromosomal inversions in these regions using PCR (Fig. 2a). We obtained a strain in which cluster I-A was fused with cluster II-C and cluster I-B was fused with cluster II-D, thereby forming two new clusters, termed cluster (A + C) and cluster (B + D) (Fig. 2a and Extended Data Fig. 3a). In the inversion strain, the piRNA gene numbers and densities were similar between the two new clusters. Using UAD-2::GFP as the fluorescence reporter for piRNA genome location, we observed that the LG IV inversion strain exhibited two smaller foci on the same chromosome per nucleus compared to the presence of a single UAD-2 focus in each pachytene stage germ cell nucleus in wild-type worms (Fig. 2b). Small RNA-seq revealed that the proportion of piRNAs from the original cluster I increased from 4% in wild-type animals to 14% in the inverted strain, approaching the proportion of piRNA gene numbers (Fig. 2c and Extended Data Fig. 3b). Most piRNAs located in cluster I exhibited over twofold increased expression, with average expression rising from ~2.9 RPM in wild-type animals to ~8.7 RPM in inverted animals (Fig. 2d–g and Extended Data Fig. 3c–f). Furthermore, the expression of piRNA genes located in clusters I-A and I-B was upregulated 2–3-fold in the inversion strain compared to the wild-type strain (Fig. 2d,f). However, piRNAs located in clusters II-C and II-D or other regions did not exhibit significant expression changes (Fig. 2e,g).

Translocation of the piRNA genes reduces piRNA expression

To test whether localization within a cluster is crucial for piRNA expression, we used CRISPR–Cas9 technology to delete a 4.2-kb segment (group B) from cluster II containing 21 actively expressed piRNA genes and inserted it into the *ttti5605* site on chromosome II (Fig. 2h). piRNA-seq showed that the group B piRNAs exhibited nearly no expression in either the deletion or the translocation strains compared to wild-type animals. In contrast, the flanking segments, groups A and C, exhibited similar piRNA expression levels to those of wild-type animals (Fig. 2i–k).

Thus, the chromosome inversion and translocation experiments implied that the clustering of piRNA genes might be an important contributor to robust piRNA expression.

Mobility properties of the H3K27me3 reader UAD-2 and the USTC complex

Fluorescence imaging revealed that UAD-2 and the USTC component TOFU-5 formed distinct subnuclear foci of approximately 1 μm^2 within each germline nucleus at 20 °C (Extended Data Fig. 4a,b). Our previous work showed that increasing temperature is detrimental to piRNA expression[16]. When the worms were cultured at 25 °C for approximately 24 h, the piRNA foci dispersed. The piRNA foci recovered upon returning the worms to 20 °C culture conditions (Extended Data Fig. 4c–f). We speculated that the clustered expression of piRNAs might be achieved through the condensation of certain transcription factors. Temperature might regulate piRNA transcription by modulating the aggregation and dispersion of piRNA transcription machinery.

First, we assessed the protein mobility of piRNA transcription factors in vivo using fluorescence recovery after photobleaching (FRAP). The rapid recovery of the photobleached UAD-2 aggregates revealed high mobility of UAD-2 in the nucleus (Fig. 3a,b). In contrast, the USTC components, including TOFU-4, TOFU-5, PRDE-1 and SNPC4, displayed negligible, if any, recovery after photobleaching (Fig. 3a,b).

https://doi.org/10.1038/s41594-025-01533-5

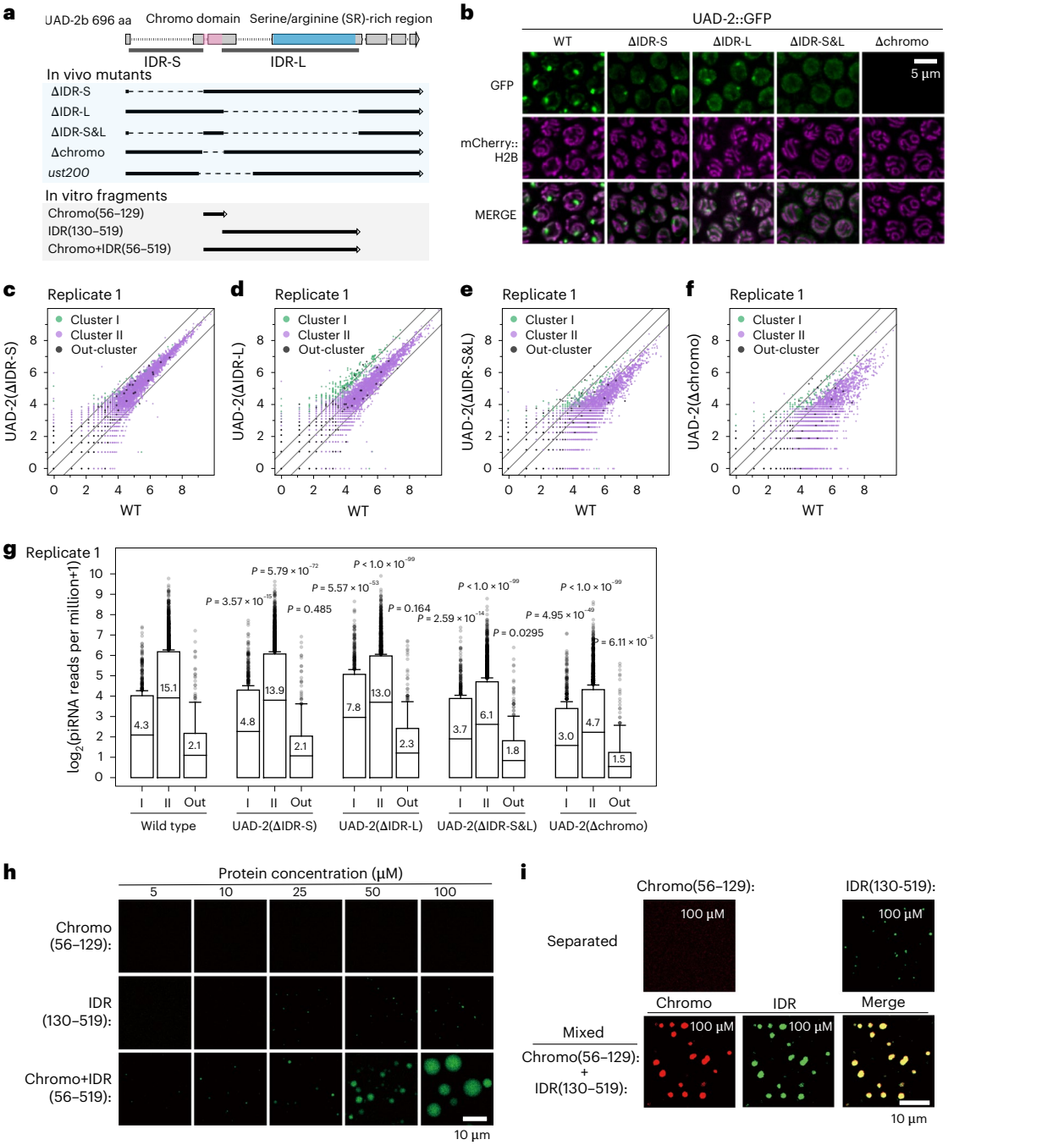

Fig. 4 | IDRs of UAD-2 have a key role in condensate formation. a, Diagram illustrating the domain structure of UAD-2. Chromo(56–129), Chromo + IDR(56–519) and IDR(130–519) indicate in vitro expressed fragments of UAD-2, respectively. **b**, Images showing the subcellular localization of the indicated UAD-2::GFP and mCherry::H2B transgenes in pachytene cells. All images were taken by the Leica Thunder imaging system and deconvoluted using Leica Application Suite X software (version 3.7.4.23463). All images are representative of more than three animals. **c**–**f**, Scatter plots displaying the expression levels of cluster I, cluster II and out-cluster piRNAs in the wild type (*x* axis) and indicated mutant (*y* axis; UAD-2(ΔIDR-S) (**c**), UAD-2(ΔIDR-L) (**d**), UAD-2(ΔIDR-S&L) (**e**) and UAD-2(Δchromo) (**f**)), based on the $\log_2$(RPM + 1) from a single biological replicate. Gray solid lines indicate reference slopes of $y = 2x$ (left), $y = x$ (center) and $y = 0.5x$ (right). **g**, Box plots revealing $\log_2$(piRNA RPM + 1) of the indicated adult animals from a single biological replicate. The box itself represents the interquartile range between 5% and 95%, thereby encompassing the middle 90% of the dataset. The central horizontal line and the adjacent numeric value within the box represent the mean value. Error bars represent the mean ± 1.5 s.d., indicating the variability of the data around the mean. Outliers are individually marked as points, representing data points that fall outside the range of mean ± 1.5 s.d. Statistical significance was determined using a paired-sample *t*-test. **h**, Images showing the liquid droplet formation of recombinant UAD-2 fragments in vitro. The incubation time before imaging for each group was 5 min. All images were taken using a Zeiss LSM 980 confocal microscope with a ×63 oil immersion lens. All images are representative of three biological replicates. **i**, Images showing the liquid droplet formation of recombinant UAD-2 fragments in vitro.

Additionally, treating germ cell nuclei with 10% 1,6-hexanediol (1,6-HD) led to rapid dispersion of UAD-2 aggregates within 5 min, whereas the USTC foci were maintained (Fig. 3c–f). The protein mobility experiments suggested that the H3K27me3 reader protein UAD-2 might have a unique function in the dynamic regulation of piRNA transcriptional condensates.

The intrinsically disordered regions have key roles in the condensate formation of UAD-2

Previous work showed that the deletion of UAD-2 reduces piRNA expression[16]. To further elucidate the impact of UAD-2, we visualized the localization of PRDE-1::GFP in germ cells during development in the *uad-2(ust200)*-null mutant. Compared to PRDE-1 foci in wild-type animals, the loss of UAD-2 significantly reduced the size and fluorescence intensity of PRDE-1::GFP foci (Extended Data Fig. 5a,b). Deep sequencing of piRNAs indicated that the overall piRNA expression levels decreased to approximately 12% of those in wild-type animals (from 170,000 RPM to 20,000 RPM) (Extended Data Fig. 5c–e). In addition, the expression levels of piRNA genes across different clusters were also significantly reduced. These data confirmed that UAD-2 is crucial for the maintenance of piRNA expression.

UAD-2 contains two intrinsically disordered regions (IDRs) and a chromodomain (Fig. 4a and Extended Data Fig. 6a). The chromodomain recognizes H3K27me3 modification. IDRs are important to direct the formation of membraneless condensates through LLPS[9]. Using CRISPR–Cas9 technology, we deleted each of these domains and determined its subcellular localization and effect on piRNA expression. The deletion of the short and long IDRs (IDR-S and IDR-L, respectively) partially disrupted UAD-2 foci, whereas the deletion of both IDRs nearly completely abolished focus formation and chromatin association (Fig. 4b). We quantified the mRNA levels of *uad-2* in these mutants using reverse transcription (RT)–qPCR and did not find a significant change in the *uad-2* mRNA level, suggesting that the deletion may not lead to *uad-2* mRNA degradation by affecting splicing and inadequately eliciting nonsense-mediated mRNA decay (Extended Data Fig. 6b). UAD-2(ΔChromo) exhibited negligible, if any, expression, suggesting that the chromodomain is required for the stability of the UAD-2 protein (Fig. 4b).

To further investigate the impact of the IDR domains of UAD-2 on USTC, we visualized mCherry::PRDE-1 in the UAD-2 IDR truncation mutants. In the *uad-2(ust200)*-null animals, PRDE-1 appeared largely dispersed within the nucleus (Extended Data Fig. 6c–e). The deletion of IDR-S led to a significant reduction in the fluorescence intensity of the major foci of PRDE-1 (corresponding to cluster II). The deletion of IDR-L and the deletion of both IDRs (ΔIDR-S&L) also caused a significant reduction in the fluorescence intensity of the major foci of PRDE-1. Moreover, we noticed the appearance of a new small focus in some germline nuclei, which might correspond to piRNA cluster I (Extended Data Fig. 6c–e). Similar to the localization of mCherry::PRDE-1, we observed a decrease in the major focus of TOFU-4::mCherry in the UAD-2 ΔIDR-L and ΔIDR-S&L mutants, as well as a new small focus (Extended Data Fig. 6f).

We conducted small RNA deep sequencing with two independent biological replicates to examine changes in piRNA expression in the UAD-2 IDR and chromodomain deletion mutants. The deletion of IDR-S resulted in a slight increase in the expression of piRNA genes in cluster I and a decrease in the expression of piRNA genes in cluster II (Fig. 4c,g and Extended Data Fig. 6g,k). The deletion of IDR-L caused an increase in piRNA gene expression in cluster I and a significant decrease in cluster II, which is consistent with the appearance of new small PRDE-1 foci and weakened PRDE-1 major foci (Fig. 4d,g and Extended Data Fig. 6h,k). Because the chromodomain is essential for UAD-2 recognition of H3K27me3 marks, deletion of the chromodomain led to a significant global decrease in piRNA expression (Fig. 4f,g and Extended Data Fig. 6j,k). These results suggest that the IDR sequences of UAD-2 have important roles in the regulation of piRNA expression.

Notably, in the UAD-2 ΔIDR-S&L mutant, the major foci of mCherry::PRDE-1 and TOFU-4::mCherry still presented yet to a less extend and new small foci appeared in some nuclei (Extended Data Fig. 6c–f). Small RNA deep sequencing revealed a significant reduction in piRNA expression in both cluster I and cluster II piRNAs, similar to the levels observed in UAD-2 ΔChromo truncation animals (Fig. 4e,g and Extended Data Fig. 6i,k). Strikingly, UAD-2 ΔIDR-S&L::GFP almost completely failed to form foci in the nucleus (Fig. 4b). We speculated that, in addition to facilitating the aggregation of USTC components on piRNA genome, UAD-2 may help to recruit other core transcription factors to start piRNA transcription. UAD-2 ΔIDR-S&L may fail to recruit core transcription factors and piRNA transcription may, therefore, be abolished.

To further investigate the role of the IDR sequence in UAD-2 in LLPS, we expressed recombinant UAD-2 segments in *Escherichia coli*, purified the proteins and conducted an in vitro phase separation assay. Neither the UAD-2 chromodomain nor IDR-L alone could efficiently elicit the formation of liquid droplets in vitro but the fusion of the chromodomain with IDR recombinant proteins induced the formation of phase-separated droplets at a 10–100 μM concentration (Fig. 4h), suggesting a synthetic effect of these two domains. Additionally, we individually expressed and purified the UAD-2 IDR-L and chromodomain and mixed them in the in vitro phase separation assay. At the protein concentration of 100 μM, when mixed together, the two domains exhibited distinct droplet formation (Fig. 4i). This result implied that interactions between the IDR-L and chromodomain might promote LLPS of UAD-2.

Collectively, these data suggested that UAD-2 may account for the mobility and phase separation ability in the condensation of piRNA transcription machinery.

GEI-17 suppresses piRNA expression

To identify piRNA transcription regulators, we conducted two forward genetic screens targeting factors that modulate UAD-2 aggregation. In pachytene germ cells, UAD-2 forms nuclear foci at 20 °C but dissipates after 24 h at 25 °C (Extended Data Fig. 4c). Using ethyl methanesulfonate (EMS) mutagenesis on UAD-2::GFP animals, we screened for mutants retaining UAD-2 foci at 25 °C and identified two *gei-17* missense alleles from ~2,000 haploid genomes (Fig. 5a–c and Extended Data Fig. 7a,b). Because GEI-17 encodes a highly conserved SUMO E3 ligase, we speculated that SUMOylation may prohibit the formation of piRNA foci (Fig. 5d). Indeed, knockdown of the SUMOylation gene *smo-1* recovered the formation of UAD-2, TOFU-4 and TOFU-5 foci at 25 °C (Fig. 5e). Consistently, GEI-17 and SMO-1 suppressed piRNA expression at 25 °C. In *gei-17* mutants or *smo-1*-knockdown animals, piRNA levels increased (Fig. 5f–h and Extended Data Fig. 7c,d). Furthermore, we performed deep sequencing of pre-piRNAs and found that, in *gei-17* mutants, pre-piRNA levels increased at 25 °C, implying the regulation of piRNA expression at the transcriptional level (Extended Data Fig. 7e,f). GFP-tagged GEI-17 primarily localized to germ cell nuclei and colocalized with chromosomes, suggesting its capability to modify potential chromatin proteins and regulate piRNA expression (Fig. 5i). GEI-17 was also localized in embryos and somatic tissues (Extended Data Fig. 7g,h). Interestingly, GEI-17 was present in the nucleolar vacuoles in oocyte cells (Fig. 5i)[59].

Thus, these data suggested that SUMOylation suppresses the aggregation of piRNA transcription machinery and piRNA production at 25 °C.

TOFU-3 is required for UAD-2 condensates and piRNA production

We conducted a second forward genetic screening to search for factors that are required for UAD-2 foci formation at 20 °C. We mutagenized UAD-2::GFP animals using EMS and isolated two *tofu-3* missense alleles and one *prde1* allele from approximately 2,000 haploid genomes, in which UAD-2 foci were depleted in germ cells at 20 °C (Fig. 6a–c and Extended Data Figs. 7a and 8a,b). A complementation assay involving multiple *tofu-3* alleles and a transgene rescue experiment confirmed that TOFU-3 is essential for the formation of UAD-2 condensates (Extended Data Fig. 8c,d). *tofu-3*, also known as ubiquitin-like protease (*ulp-5*), encodes a conserved deSUMOylation peptidase located

https://doi.org/10.1038/s41594-025-01533-5

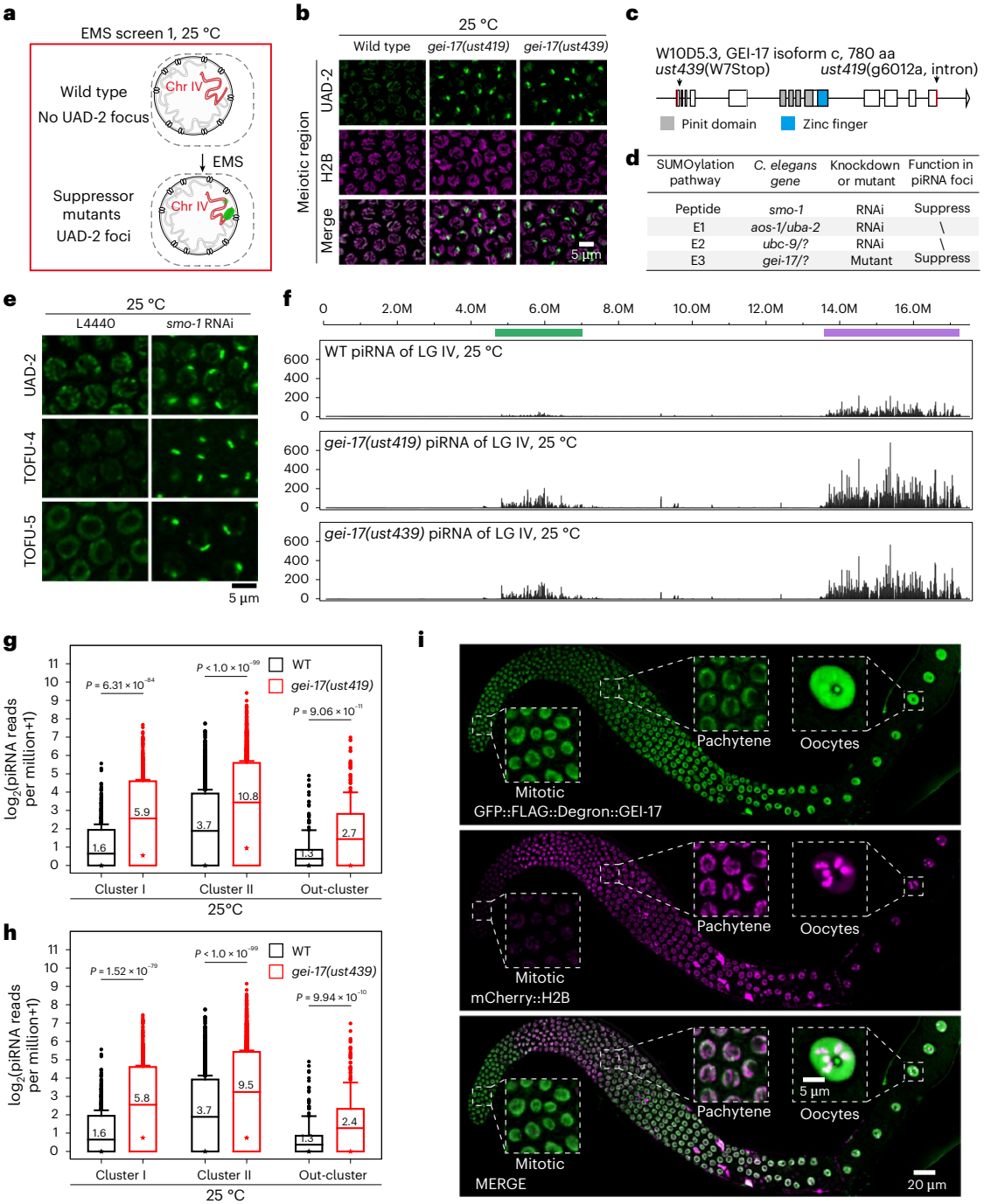

Fig. 5 | Forward genetic screening identifies GEI-17 suppressing piRNA expression. a, Schematic diagram displaying the forward genetic screening for UAD-2 focus suppressors in *C. elegans* germline nuclei at 25 °C. **b**, Images showing pachytene cells of the indicated adult animals grown at 25 °C. All images were taken by the Leica Thunder imaging system and deconvoluted using Leica Application Suite X software (version 3.7.4.23463). All images are representative of more than three animals. **c**, Diagram illustrating the *gei-17* exon and domain structure. The *ust439* allele changes tryptophan 7 to a stop codon and is likely a null allele. *ust419* modifies the second base of the last intron. **d**, Summary of the SUMOylation pathway in *C. elegans*. **e**, Images showing pachytene cells of the dsRNA-treated animals grown at 25 °C. **f**, Graphs presenting the expression levels of total piRNAs from LG IV of the indicated adult animals grown at 25 °C from a single biological replicate, normalized as RPM + 1. The *x* axis unit is base pairs (bp), where 'M' denotes million. **g**,**h**, Box plots revealing $\log_2$(piRNA RPM + 1) of the indicated adult animals (*gei-17(ust419)* (**g**) and *gei-17(ust439)* (**h**)) from a single biological replicate. The box itself represents the interquartile range between 5% and 95%, thereby encompassing the middle 90% of the dataset. The central horizontal line and the adjacent numeric value within the box represent the mean value. The star within the box represents the median value. Error bars represent the mean ± 1.5 s.d., indicating the variability of the data around the mean. Outliers are individually marked as points, representing data points that fall outside the range of mean ± 1.5 s.d. Statistical significance was determined using a paired-sample *t*-test. **i**, Images displaying the germline of adult animals. GFP::FLAG::Degron::GEI-17 (green) partially colocalized with the chromatin marker mCherry::H2B (magenta).

on LG I (Fig. 6c and Extended Data Fig. 8e). Knockdown of *ulp* family members showed that TOFU-3/ULP-5 is likely the only deSUMOylation peptidase involved in UAD-2 focus formation (Extended Data Fig. 8f). Small RNA-seq indicated that TOFU-3 is specifically required for the expression of the two clusters but not the out-cluster-localized piRNA genes (Fig. 6d,e and Extended Data Fig. 8g,h).

We generated an in situ 3×FLAG::GFP-tagged TOFU-3 by CRISPR–Cas9 technology. TOFU-3 was predominantly expressed in mitotic and transition zones, was weakly expressed in early pachytene cells and formed nuclear foci that colocalized with PRDE-1 (Fig. 6f,g). The mutation of *prde1* prevents the formation of TOFU-3 foci (Fig. 6h). On the other hand, the formation of TOFU-4, TOFU-5 and PRDE-1 foci also depends on TOFU-3 (Fig. 6i,j and Extended Data Fig. 9a,b). These findings suggest a mutual dependency between TOFU-3 and the USTC complex for localization, indicating that TOFU-3 may be part of the piRNA transcription machinery. Although identified in a genome-wide RNAi screen for piRNA expression, TOFU-3 was not detected in PRDE-1 or TOFU-5 IP–mass spectrometry or in SNPC4 yeast-two-hybrid assays[14,60]. Further investigation using proteomics or yeast-two-hybrid methods could clarify how TOFU-3 is recruited to piRNA foci.

To assess the role of TOFU-3-mediated deSUMOylation in piRNA transcription, we performed *smo-1* RNAi in tofu-3 mutants. *smo-1* depletion restored UAD-2 focus formation and significantly increased piRNA expression (Fig. 6k,l and Extended Data Fig. 9c).

In wild-type nuclei, UAD-2 is enriched at piRNA gene clusters with minimal colocalization to other chromatin regions. In *tofu-3* mutants, UAD-2 aggregation is lost, showing increased global chromatin association compared to the wild type (Extended Data Fig. 9d–f). These findings suggest that TOFU-3 loss disrupts UAD-2 condensation but not its chromatin-binding ability.

SUMOylation coordinates piRNA expression

At 20 °C, wild-type germ cells displayed one explicit UAD-2 focus, corresponding to cluster II piRNA loci, in pachytene nuclei. However, we did not observe a second explicit UAD-2 focus corresponding to cluster I piRNA loci (Figs. 1b and 7a). Strikingly, *gei-17* mutants displayed an additional pronounced UAD-2 focus corresponding to cluster I piRNA loci (Fig. 7b,c). Consistently, cluster I piRNAs were substantially upregulated in *gei-17* mutants at 20 °C (Fig. 7d–f). Similarly, *smo-1* knockdown led to the formation of two UAD-2 foci and USTC foci in each pachytene nucleus (Extended Data Fig. 10a–f) and a significant upregulation of cluster I piRNA levels (Extended Data Fig. 10g,h).

To further investigate the role of SUMOylation in regulating piRNA expression, we introduced a single-copy transgene with strong *mex5* promoter-driven mCherry::TOFU-3 into the germline of wild-type worms. The introduction of *mex5p::*mCherry::TOFU-3 resulted in the overexpression of TOFU-3 (Extended Data Fig. 10i), increased global pre-piRNA levels at 25 °C (Extended Data Fig. 10j) and increased UAD-2 binding to the two piRNA clusters when cultured at 20 °C (Fig. 7g). Therefore, the effects of the loss of the SUMOylation E3 ligase GEI-17 or the overexpression of the SUMOylation peptidase TOFU-3 at 25 °C suggest that SUMOylation could regulate piRNA expression at the transcriptional level.

Our data indicate that, at 20 °C, SUMOylation suppresses cluster I piRNA expression (Fig. 7e,f,h), whereas, at 25 °C, SUMOylation suppresses piRNA expression from both clusters (Fig. 5g,h).

These findings indicate that SUMOylation may have a crucial role in repressing piRNA gene expression.

To further test the regulatory role of SUMOylation in piRNA transcription, we conducted FRAP and 1,6-HD treatment experiments upon knocking down *smo-1*. At 20 °C, reducing SUMOylation levels by *smo-1* RNAi led to less mobility of UAD-2 foci (Extended Data Fig. 10k–m), suggesting that SUMOylation increased UAD-2 mobility. Although the predicted UAD-2 IDRs were shown to promote robust USTC foci formation and efficient piRNA expression, the density of piRNA genes, SUMOylation and protein–protein interactions may all facilitate the assembly of USTC foci and piRNA expression and may even have more important roles than condensate formation per se.

Together, these data suggested that GEI-17-mediated SUMOylation and TOFU-3-mediated deSUMOylation bilaterally modulate the aggregation of piRNA transcription machineries and coordinate piRNA expression (Fig. 7i).

Discussion

This study demonstrated that piRNA gene clustering density is crucial for piRNA expression in *C. elegans*, supported by cross-species comparisons and chromosome manipulation assays. UAD-2 undergoes LLPS to form dynamic condensates at piRNA clusters, with SUMOylation regulating their assembly and dynamics. TOFU-3, a SUMO protease, is essential for UAD-2 focus formation and piRNA production, while the SUMO E3 ligase GEI-17 opposes condensate integrity. These findings suggest that regulated SUMOylation serves as a molecular switch controlling UAD-2 aggregation and piRNA transcription (Fig. 7i). In summary, we showed that piRNA gene density, UAD-2 phase separation properties and SUMOylation status constitute an intricate regulatory circuit that cooperatively orchestrates piRNA transcription factory and piRNA production. We proposed that UAD-2 condensates at dense piRNA clusters and enhances transcription, a process fine-tuned by SUMOylation (Fig. 8).

piRNA transcription from the heterochromatinized genome

The mechanism of transcription from heterochromatic regions remains poorly understood. In *Drosophila* ovarian germ cells, piRNAs are produced from dual-strand clusters embedded in heterochromatin

Fig. 6 | TOFU-3 is required for UAD-2 condensate formation and piRNA production. a, Schematic diagram displaying the forward genetic screening for mutants without UAD-2 focus in *C. elegans* germline nuclei at 20 °C. **b**, Images showing pachytene cells of the indicated adult animals grown at 20 °C. All images were taken by the Leica Thunder imaging system and deconvoluted using Leica Application Suite X software (version 3.7.4.23463). All images are representative of more than three animals. **c**, Diagram illustrating the *ulp-5/tofu-3* exon and domain structure. The alleles *ust238*, *ust235* and *tm3068* are highlighted. *tm3068* was likely a null allele and was used as a reference allele. **d**, Graphs presenting the expression levels of total piRNAs from LG IV of the indicated adult animals grown at 20 °C from a single biological replicate, normalized as RPM + 1. The *x* axis unit is base pairs (bp), where 'M' denotes million. **e**, Box plots revealing $\log_2$(piRNA RPM+1) of the indicated adult animals from a single biological replicate. The box itself represents the interquartile range between 5% and 95%, thereby encompassing the middle 90% of the dataset. The central horizontal line represents the mean value. Error bars represent the mean ± 1.5 s.d., indicating the variability of the data around the mean. Outliers are individually marked as points, representing data points that fall outside the range of mean ± 1.5 s.d. Statistical significance was determined using a paired-sample *t*-test. **f**, Images displaying the germline of adult animals. Dashed boxes indicate the regions magnified in the panels below. TOFU-3::GFP::3×FLAG (green) partially colocalized with the chromatin marker mCherry::H2B (magenta). All images are representative of more than three animals. **g**, Images showing colocalization of TOFU-3::GFP::3×FLAG (green) with mCherry::PRDE-1 (magenta) in mitotic and meiotic germline nuclei of adult animals. All images are representative of more than three animals. **h**, Images of representative meiotic germline nuclei of the indicated adult animals. TOFU-3::GFP::3×FLAG failed to form piRNA foci in *prde1(mj207)* animals. All images are representative of more than three animals. **i**,**j**, Images of representative meiotic germline nuclei of the indicated adult animals. TOFU-4::GFP (**i**) and TOFU-5::GFP (**j**) failed to form piRNA foci in *tofu-3(tm3068)* animals. **k**,**l**, Subcellular localization of UAD-2::GFP and mCherry::H2B in pachytene cells from wild-type worms fed L4440 and *tofu-3* (*tofu-3(ust235)* (**k**) and *tofu-3(tm3068)* (**l**)) mutant worms fed L4440 and *smo-1* dsRNA bacteria. All images are representative of more than three animals.

https://doi.org/10.1038/s41594-025-01533-5

marked by H3K9me3, which is recognized by the chromo protein Rhino. Here, we found a similar clustering mechanism to maintain efficient piRNA transcription from H3K27me3-enriched genomic loci, which are recognized by the chromo protein UAD-2, in *C. elegans*. The unique biophysical properties of UAD-2, including high intrinsic disorder and mobility, allow it to access and dynamically regulate clustered piRNA loci. Patel et al. also reported from Hi-C data that piRNA clusters could form transcription hubs through long-distance interactions[61]. Together, these results suggest that eukaryotes may use a universally conserved strategy to boost piRNA transcription through the spatial aggregation of piRNA genes to enhance gene density and proximity.

Phase separation regulates transcriptional condensates

Transcription occurs in a compartmentalized manner through 'transcription factories' to facilitate subnuclear localized transcription factors. Specific genomic clustering of short noncoding RNA genes may promote compartmentalization and efficient gene expression. Thus, piRNA transcription condensates provide an ideal model to dissect the mechanism(s) by which phase separation regulates transcription in vivo and how chromatin organization and posttranslational modifications (for example, SUMOylation) orchestrate gene expression. Integrative application of multidisciplinary approaches to address these questions will provide deeper mechanistic insights into the phase-separated control of noncoding RNA synthesis and transcription.

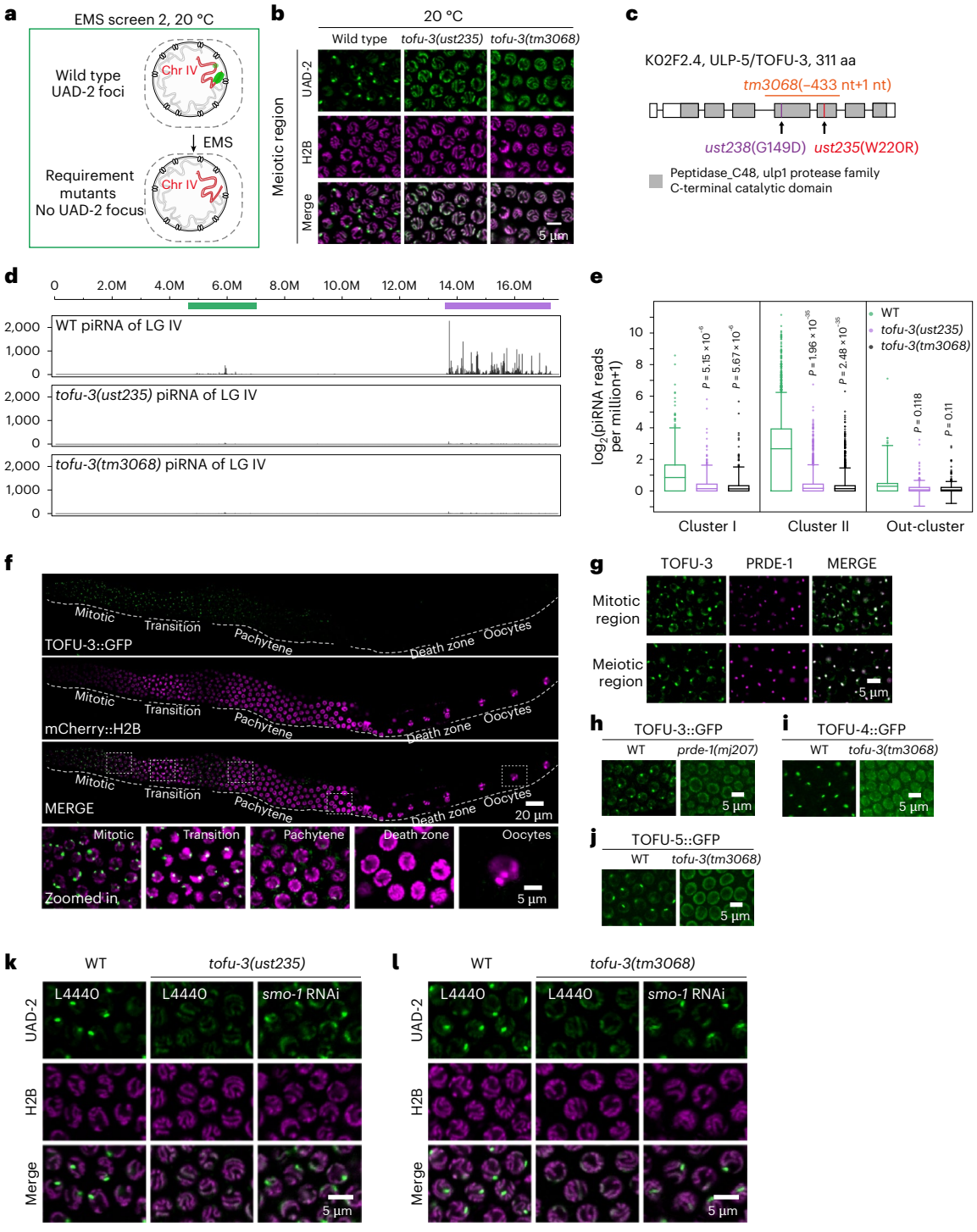

https://doi.org/10.1038/s41594-025-01533-5

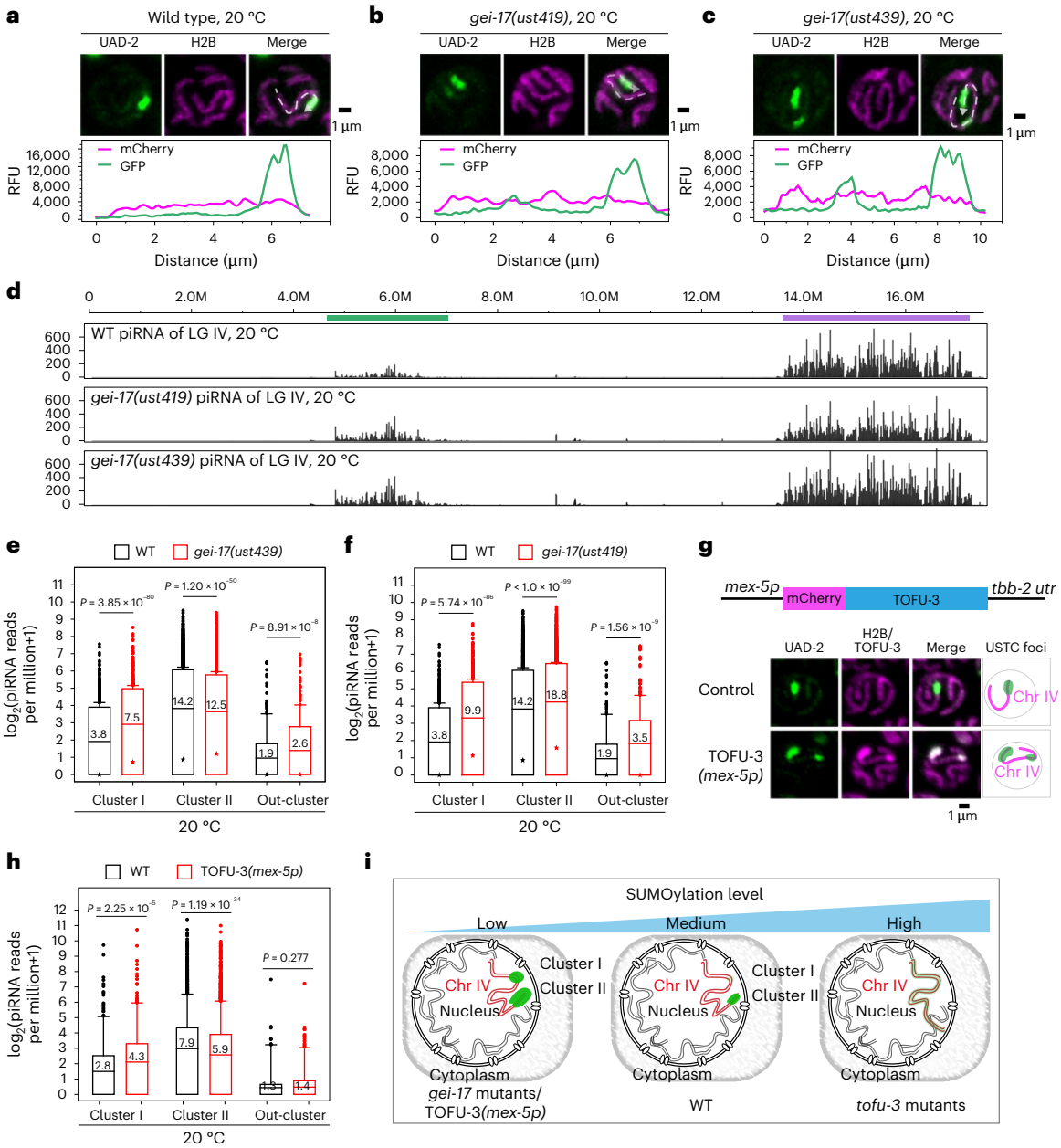

Fig. 7 | SUMOylation suppresses cluster I piRNA expression. a–**c**, Top: subcellular localization of UAD-2::GFP with mCherry::H2B in pachytene cells of the indicated animals (wild type (**a**), *gei-17(ust419)* (**b**) and *gei-17(ust439)* (**c**)) maintained at 20 °C. Bottom: RFU as indicated by dashed lines along chromosome IV in the top panel. All images were taken by the Leica Thunder imaging system and deconvoluted using Leica Application Suite X software (version 3.7.4.23463). All images are representative of more than three animals. **d**, Expression levels of total piRNAs from LG IV of the indicated adult animals maintained at 20 °C from a single biological replicate, normalized as RPM + 1. The *x* axis unit is base pairs (bp), where 'M' denotes million. **e**,**f**, Box plots presenting $\log_2$(piRNA RPM + 1) of the indicated adult animals (*gei-17(ust439)* (**e**) and *gei-17(ust419)* (**f**)) from a single biological replicate. The box itself represents the interquartile range between 5% and 95%, thereby encompassing the middle 90% of the dataset. The central horizontal line and the adjacent numeric value within the box represent the mean value. The star within the box represents the median value. Error bars represent the mean ± 1.5 s.d., indicating the variability of the data around the mean. Outliers are individually marked as points, representing data points that fall outside the range of mean ± 1.5 s.d. Statistical significance was determined using a paired-sample *t*-test. **g**, Top: diagram illustrating mCherry::TOFU-3 by the *mex5* promoter and *tbb2* untranslated region (TOFU-3(*mex5p*)). Bottom: subcellular localization of UAD-2::GFP with mCherry::H2B/mCherry::TOFU-3 in pachytene cells of the indicated animals maintained at 20 °C. **h**, Box plots presenting $\log_2$(piRNA RPM + 1) of the indicated adult animals. Statistical significance was determined using a paired-sample *t*-test. **i**, Schematic diagram of the SUMOylation level regulating UAD-2::GFP and USTC complex condensation.

SUMOylation and piRNA production

SUMOylation regulates LLPS through multivalent interactions mediated by SUMO and SUMO-interacting motifs (SIMs), promoting the formation of biomolecular condensates[42,46,62]. In vitro experiments showed that combining polySUMO and polySIM results in phase-separated droplets. In vivo observations revealed that stress could induce SUMOylation and the assembly of biomolecular condensates, such as the promyelocytic leukemia nuclear body[44,63]. Our study demonstrated that SUMOylation in *C. elegans* germline cells suppresses piRNA transcription condensate formation, inhibiting piRNA transcription.

https://doi.org/10.1038/s41594-025-01533-5

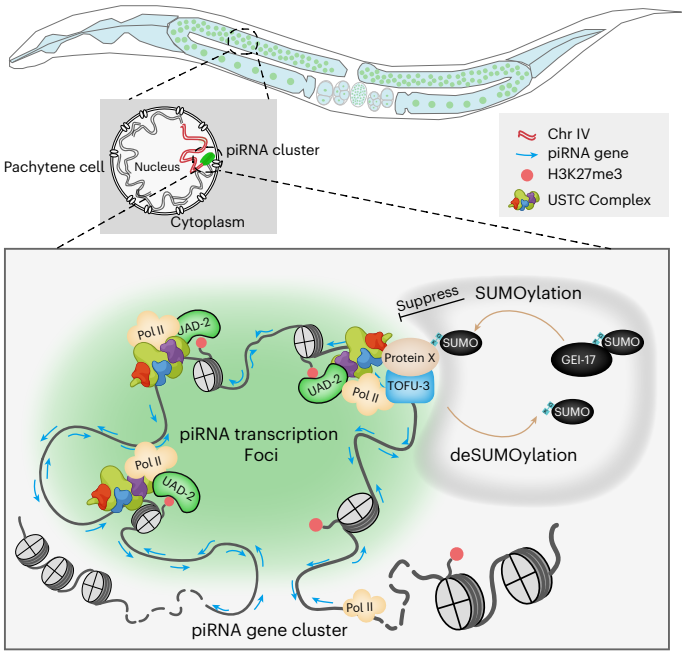

Fig. 8 | A working model for piRNA transcription in *C. elegans*. In *C. elegans*, densely clustered piRNA genes facilitate the assembly of UAD-2 condensates, which in turn actively recruit the USTC complex and Pol II and subsequently initiate piRNA transcription. Concurrently, the SUMO E3 ligase GEI-17 antagonizes piRNA condensate integrity and TOFU-3-mediated deSUMOylation promotes piRNA condensate formation and piRNA biogenesis.

We propose that SUMOylation of diverse proteins induces varying physicochemical changes, with polySUMO and monoSUMO exerting distinct effects on condensate formation. Using *C. elegans* as a model to study SUMOylation's role in regulating biomolecular condensates and transcription offers valuable insights into its in vivo biological functions.

Previous studies in both *Drosophila* and *C. elegans* identified the SUMOylation process as crucial for piRNA-mediated transcriptional silencing by suppressing target genes[47–51]. However, our findings suggest that SUMOylation can also modulate piRNA production. While SUMOylation inhibits piRNA transcription, the specific deSUMOylation enzyme, TOFU-3, promotes piRNA transcription. Thus, SUMOylation may exert different regulatory roles across these separate processes. How SUMOylation serves as a repressive force in RNA polymerase II (Pol II)-driven piRNA expression processes requires further exploration.

piRNAs are noncoding small RNAs with specialized functions during distinct phases of germ cell development, necessitating meticulous transcriptional control. At developmental stages, it becomes imperative to precisely modulate piRNA transcription. In such scenarios, the transient binding affinity of UAD-2 combined with the suppressive effect of SUMOylation can effectively terminate piRNA transcription. Under specific environmental stresses, the inherent mobility of UAD-2 and the effects of SUMOylation may facilitate the organism's adaptation through gene expression modulation.

Limitations and perspectives of the study

While our study has advanced the understanding of piRNA regulation, several key questions remain. Identifying the substrate(s) of SUMOylation will illuminate the key molecular switches governing compartment dynamics. In addition, TOFU-3-mediated deSUMOylation and the UAD-2 IDR may promote USTC foci formation through different mechanisms. The loss of TOFU-3 nearly eliminates PRDE-1 foci in both the mitotic and meiotic zones. However, in the UAD-2 ΔIDR-S&L mutant, the intensity of PRDE-1 in the piRNA foci was modestly reduced and a second smaller PRDE-1 focus appeared in some nuclei. The identification of the substrates for TOFU-3 may help to illustrate these differences. Although TOFU-3 colocalizes with USTC at piRNA clusters during mitotic and early meiotic germ cells, we currently lack evidence showing that TOFU-3 directly interacts with UAD-2 or USTC components. We speculated that UAD-2 or USTC components may not be the direct substrate of TOFU-3. Some other factors, which requires identification, may be involved in SUMOylation and piRNA regulation. Elucidating the interaction and regulatory relationship involving the histone reader UAD-2, the USTC complex and the core transcription machinery is crucial for understanding the mechanism of piRNA transcription. Additionally, investigating whether and how specific transcription factors are involved in piRNA transcription will greatly benefit the understanding of heterochromatic genome expression.

Online content

Any methods, additional references, Nature Portfolio reporting summaries, source data, extended data, supplementary information, acknowledgements, peer review information; details of author contributions and competing interests; and statements of data and code availability are available at https://doi.org/10.1038/s41594-025-01533-5.

References

1. Vagin, V. V. et al. A distinct small RNA pathway silences selfish genetic elements in the germline. *Science* **313**, 320–324 (2006).
2. Aravin, A. et al. A novel class of small RNAs bind to MILI protein in mouse testes. *Nature* **442**, 203–207 (2006).
3. Girard, A., Sachidanandam, R., Hannon, G. J. & Carmell, M. A. A germline-specific class of small RNAs binds mammalian Piwi proteins. *Nature* **442**, 199–202 (2006).
4. Lau, N. C. et al. Characterization of the piRNA complex from rat testes. *Science* **313**, 363–367 (2006).
5. Grivna, S. T., Beyret, E., Wang, Z. & Lin, H. F. A novel class of small RNAs in mouse spermatogenic cells. *Genes Dev.* **20**, 1709–1714 (2006).
6. Ashe, A. et al. piRNAs can trigger a multigenerational epigenetic memory in the germline of *C. elegans*. *Cell* **150**, 88–99 (2012).
7. Bagijn, M. P. et al. Function, targets, and evolution of *Caenorhabditis elegans* piRNAs. *Science* **337**, 574–578 (2012).
8. Wang, X., Ramat, A., Simonelig, M. & Liu, M. F. Emerging roles and functional mechanisms of Piwi-interacting RNAs. *Nat. Rev. Mol. Cell Biol.* **24**, 123–141 (2023).
9. Wright, P. E. & Dyson, H. J. Intrinsically disordered proteins in cellular signalling and regulation. *Nat. Rev. Mol. Cell Biol.* **16**, 18–29 (2015).
10. Weick, E. M. et al. PRDE-1 is a nuclear factor essential for the biogenesis of Ruby motif-dependent piRNAs in *C. elegans*. *Genes Dev.* **28**, 783–796 (2014).
11. Gu, W. et al. CapSeq and CIP-TAP identify Pol II start sites and reveal capped small RNAs as *C. elegans* piRNA precursors. *Cell* **151**, 1488–1500 (2012).
12. Cecere, G., Zheng, G. X., Mansisidor, A. R., Klymko, K. E. & Grishok, A. Promoters recognized by forkhead proteins exist for individual 21U-RNAs. *Mol. Cell* **47**, 734–745 (2012).
13. Beltran, T. et al. Comparative epigenomics reveals that RNA polymerase II pausing and chromatin domain organization control nematode piRNA biogenesis. *Dev. Cell* **48**, 793–810 (2019).
14. Weng, C. et al. The USTC co-opts an ancient machinery to drive piRNA transcription in *C. elegans*. *Genes Dev.* **33**, 90–102 (2019).
15. Kasper, D. M., Wang, G., Gardner, K. E., Johnstone, T. G. & Reinke, V. The *C. elegans* SNAPc component SNPC-4 coats piRNA domains and is globally required for piRNA abundance. *Dev. Cell* **31**, 145–158 (2014).
16. Huang, X. et al. A chromodomain protein mediates heterochromatin-directed piRNA expression. *Proc. Natl Acad. Sci. USA* **118**, e2103723118 (2021).

17. Zhang, G., Zheng, C., Ding, Y. H. & Mello, C. Casein kinase II promotes piRNA production through direct phosphorylation of USTC component TOFU-4. *Nat. Commun.* **15**, 2727 (2024).
18. Paniagua, N., Roberts, C. J., Gonzalez, L. E., Monedero-Alonso, D. & Reinke, V. The upstream sequence transcription complex dictates nucleosome positioning and promoter accessibility at piRNA genes in the *C. elegans* germ line. *PLoS Genet.* **20**, e1011345 (2024).
19. Rangan, P. et al. piRNA production requires heterochromatin formation in *Drosophila*. *Curr. Biol.* **21**, 1373–1379 (2011).
20. Wei, X., Eickbush, D. G., Speece, I. & Larracuente, A. M. Heterochromatin-dependent transcription of satellite DNAs in the *Drosophila melanogaster* female germline. *eLife* **10**, e62375 (2021).
21. Zhang, G. et al. Co-dependent assembly of *Drosophila* piRNA precursor complexes and piRNA cluster heterochromatin. *Cell Rep.* **24**, 3413–3422 (2018).
22. ElMaghraby, M. F. et al. A heterochromatin-specific RNA export pathway facilitates piRNA production. *Cell* **178**, 964–979.e20 (2019).
23. Andersen, P. R., Tirian, L., Vunjak, M. & Brennecke, J. A heterochromatin-dependent transcription machinery drives piRNA expression. *Nature* **549**, 54–59 (2017).
24. Le Thomas, A. et al. Transgenerationally inherited piRNAs trigger piRNA biogenesis by changing the chromatin of piRNA clusters and inducing precursor processing. *Genes Dev.* **28**, 1667–1680 (2014).
25. Mohn, F., Sienski, G., Handler, D. & Brennecke, J. The Rhino–Deadlock–Cutoff complex licenses noncanonical transcription of dual-strand piRNA clusters in *Drosophila*. *Cell* **157**, 1364–1379 (2014).
26. Klattenhoff, C. et al. The *Drosophila* HP1 homolog Rhino is required for transposon silencing and piRNA production by dual-strand clusters. *Cell* **138**, 1137–1149 (2009).
27. Kneuss, E. et al. Specialization of the *Drosophila* nuclear export family protein Nxf3 for piRNA precursor export. *Genes Dev.* **33**, 1208–1220 (2019).
28. Lafontaine, D. L. J., Riback, J. A., Bascetin, R. & Brangwynne, C. P. The nucleolus as a multiphase liquid condensate. *Nat. Rev. Mol. Cell Biol.* **22**, 165–182 (2021).
29. Gilks, N. et al. Stress granule assembly is mediated by prion-like aggregation of TIA-1. *Mol. Biol. Cell* **15**, 5383–5398 (2004).
30. Saitoh, N. et al. Proteomic analysis of interchromatin granule clusters. *Mol. Biol. Cell* **15**, 3876–3890 (2004).
31. Shin, Y. & Brangwynne, C. P. Liquid phase condensation in cell physiology and disease. *Science* **357**, eaaf4382 (2017).
32. Banani, S. F., Lee, H. O., Hyman, A. A. & Rosen, M. K. Biomolecular condensates: organizers of cellular biochemistry. *Nat. Rev. Mol. Cell Biol.* **18**, 285–298 (2017).
33. Liu, Y., Yao, Z., Lian, G. & Yang, P. Biomolecular phase separation in stress granule assembly and virus infection. *Acta Biochim. Biophy. Sin.* **55**, 1099–1118 (2023).
34. Guo, G., Wang, X., Zhang, Y. & Li, T. Sequence variations of phase-separating proteins and resources for studying biomolecular condensates. *Acta Biochim. Biophy. Sin.* **55**, 1119–1132 (2023).
35. Hnisz, D., Shrinivas, K., Young, R. A., Chakraborty, A. K. & Sharp, P. A. A phase separation model for transcriptional control. *Cell* **169**, 13–23 (2017).
36. Lu, Y. et al. Phase separation of TAZ compartmentalizes the transcription machinery to promote gene expression. *Nat. Cell Biol.* **22**, 453–464 (2020).
37. Li, C., Li, Z., Wu, Z. & Lu, H. Phase separation in gene transcription control. *Acta Biochim. Biophy. Sin.* **55**, 1052–1063 (2023).
38. Lallemand-Breitenbach, V. & de Thé, H. PML nuclear bodies: from architecture to function. *Curr. Opin. Cell Biol.* **52**, 154–161 (2018).
39. Yamazaki, T. et al. Functional domains of NEAT1 architectural lncRNA induce paraspeckle assembly through phase separation. *Mol. Cell* **70**, 1038–1053 (2018).
40. Spector, D. L. & Lamond, A. I. Nuclear speckles. *Cold Spring Harb. Perspect. Biol.* **3**, a000646 (2011).
41. Nizami, Z., Deryusheva, S. & Gall, J. G. The Cajal body and histone locus body. *Cold Spring Harb. Perspect. Biol.* **2**, a000653 (2010).
42. Vertegaal, A. C. O.Signalling mechanisms and cellular functions of SUMO. *Nat. Rev. Mol. Cell. Biol.* **23**, 715–731 (2022).
43. Keiten-Schmitz, J., Röder, L., Hornstein, E., Müller-McNicoll, M. & Müller, S. SUMO: glue or solvent for phase-separated ribonucleoprotein complexes and molecular condensates? *Front. Mol. Biosci.* **8**, 673038 (2021).
44. Banani, S. F. et al. Compositional control of phase-separated cellular bodies. *Cell* **166**, 651–663 (2016).
45. Leonen, C. J. A. et al. Sumoylation of the human histone H4 tail inhibits p300-mediated transcription by RNA polymerase II in cellular extracts. *eLife* **10**, e67952 (2021).
46. Cheng, X. Protein SUMOylation and phase separation: partners in stress? *Trends Biochem. Sci.* **48**, 417–419 (2023).
47. Andreev, V. I. et al. Panoramix SUMOylation on chromatin connects the piRNA pathway to the cellular heterochromatin machinery. *Nat. Struct. Mol. Biol.* **29**, 130–142 (2022).
48. Kim, H. et al. HDAC1 SUMOylation promotes Argonaute-directed transcriptional silencing in *C. elegans*. *eLife* **10**, e63299 (2021).
49. Kim, H. et al. PIE-1 SUMOylation promotes germline fates and piRNA-dependent silencing in *C. elegans*. *eLife* **10**, e63300 (2021).
50. Ninova, M. et al. The SUMO Ligase Su(var)2-10 controls hetero- and euchromatic gene expression via establishing H3K9 trimethylation and negative feedback regulation. *Mol. Cell* **77**, 571–585 (2020).
51. Ninova, M. et al. Su(var)2-10 and the SUMO pathway link piRNA-guided target recognition to chromatin silencing. *Mol. Cell* **77**, 556–570 (2020).
52. Ruby, J. G. et al. Large-scale sequencing reveals 21U-RNAs and additional microRNAs and endogenoussiRNAs in C. elegans. *Cell* **127**, 1193–1207 (2006).
53. Bilgir, C., Dombecki, C. R., Chen, P. F., Villeneuve, A. M. & Nabeshima, K. Assembly of the synaptonemal complex is a highly temperature-sensitive process that is supported by PGL-1 during *Caenorhabditis elegans* meiosis. *G3 (Bethesda)* **3**, 585–595 (2013).
54. Choi, C. P. et al. SNPC-1.3 is a sex-specific transcription factor that drives male piRNA expression in *C. elegans*. *eLife* **10**, e60681 (2021).
55. Cornes, E. et al. piRNAs initiate transcriptional silencing of spermatogenic genes during *C. elegans* germline development. *Dev. Cell* **57**, 180–196 (2022).
56. Pastore, B., Hertz, H. L. & Tang, W. Comparative analysis of piRNA sequences, targets and functions in nematodes. *RNA Biol.* **19**, 1276–1292 (2022).
57. Priyadarshini, M., Ni, J. Z., Vargas-Velazquez, A. M., Gu, S. G. & Frøkjær-Jensen, C. Reprogramming the piRNA pathway for multiplexed and transgenerational gene silencing in *C. elegans*. *Nat. Methods* **19**, 187–194 (2022).
58. Chen, X. et al. Dual sgRNA-directed gene knockout using CRISPR/Cas9 technology in *Caenorhabditis elegans*. *Sci. Rep.* **4**, 7581 (2014).
59. Xu, D. et al. rRNA intermediates coordinate the formation of nucleolar vacuoles in *C. elegans*. *Cell Rep.* **42**, 112915 (2023).
60. Goh, W. S. et al. A genome-wide RNAi screen identifies factors required for distinct stages of *C. elegans* piRNA biogenesis. *Genes Dev.* **28**, 797–807 (2014).
61. Patel, L. et al. Dynamic reorganization of the genome shapes the recombination landscape in meiotic prophase. *Nat. Struct. Mol. Biol.* **26**, 164–174 (2019).

62. Chang, H. M. & Yeh, E. T. H. SUMO: from bench to bedside. *Physiol. Rev.* **100**, 1599–1619 (2020).
63. Shen, T. H., Lin, H. K., Scaglioni, P. P., Yung, T. M. & Pandolfi, P. P. The mechanisms of PML-nuclear body formation. *Mol. Cell* **24**, 331–339 (2006).

Publisher's note Springer Nature remains neutral with regard to jurisdictional claims in published maps and institutional affiliations.

Springer Nature or its licensor (e.g. a society or other partner) holds exclusive rights to this article under a publishing agreement with the author(s) or other rightsholder(s); author self-archiving of the accepted manuscript version of this article is solely governed by the terms of such publishing agreement and applicable law.

© The Author(s), under exclusive licence to Springer Nature America, Inc. 2025

Methods

Strains

Bristol strain N2 was used as the standard wild-type strain. All strains were grown at 20 °C unless otherwise specified. For the heat stress treatment, worms were cultured at 25 °C. The strains used in this study are listed in Supplementary Table 1.

Construction of deletion mutants and chromosome editing technology

For gene deletions, triple or quadruple sgRNA-guided chromosome deletion was conducted as previously described[58]. To construct sgRNA expression vectors, the 20-bp unc119 sgRNA guide sequence in the pU6::unc119 sgRNA(F + E) vector was replaced with different sgRNA guide sequences. Addgene plasmid 47549 was used to express the Cas9 II protein. Plasmid mixtures containing 30 ng μl^{-1} of each of the three or four sgRNA expression vectors, 50 ng μl^{-1} Cas9 II-expressing plasmid and 5 ng μl^{-1} pCFJ90 were coinjected into UAD-2::GFP::3×FLAG (ustIS151) animals. Deletion mutants were screened by PCR amplification and confirmed by sequencing. The sgRNA sequences are listed in Supplementary Table 2.

Dual sgRNA-mediated chromosome inversion and translocation were conducted as described previously[64]. Inversion and translocation mutants were screened by PCR amplification and confirmed by sequencing. The sgRNA sequences are listed in Supplementary Table 3.

Construction of plasmids and transgenic strains

For the in situ transgene expressing GFP::3×FLAG-tagged TOFU-4, SNPC4, PRDE-1 or TOFU-3, a GFP::3×FLAG region was PCR-amplified from SHG326 genomic DNA. The coding sequence of GFP::3×FLAG was inserted before the stop codon using the CRISPR–Cas9 system. The sgRNA target sequences are listed in Supplementary Table 2. The ClonExpress MultiS one-step cloning kit (Vazyme, C113-02) was used to connect these fragments with the vector, which was amplified with 5′-TGT GAA ATT GTT ATC CGC TGG -3′ and 5′- CAC ACG TGC TGG CGT TAC C -3′ from L4440. The injection mix contained PDD162 (50 ng μl^{-1}), repair plasmid (50 ng μl^{-1}), pCFJ90 (5 ng μl^{-1}) and two sgRNAs (30 ng μl^{-1}). The mix was injected into young adult N2 animals. The transgenes were integrated into the *C. elegans* chromosome by the CRISPR–Cas9 system.

Forward genetic screening

Forward genetic screening experiments were conducted as previously described[65]. Briefly, to identify the factors that can negatively or positively regulate UAD-2 focus formation, we mutagenized GFP::UAD-2 animals by EMS and searched for mutants that either reformed UAD-2 foci at 25 °C or depleted UAD-2 foci at 20 °C by clonal screening. The F_2 progeny worms were visualized under a fluorescence microscope at the gravid adult stage. Mutants revealing UAD-2 foci at 25 °C or no UAD-2 foci at 20 °C were selected. Both *gei-17* and *tofu-3* were identified by single-nucleotide polymorphism mapping followed by resequencing of the genome.

RNAi

RNAi experiments were performed at 20 °C or 25 °C by placing synchronized embryos on feeding plates as previously described[66]. HT115 bacteria expressing the empty vector L4440 (a gift from A. Fire) were used as controls. Bacterial clones expressing double-stranded RNAs (dsRNAs) were obtained from the Ahringer RNAi library and sequenced to verify their identity. All RNAi feeding experiments were performed for one generation from L1 to the gravid adult stage. Images were collected using a Leica DM4B microscope with a Leica Thunder image-processing system.

FRAP

FRAP experiments were performed using a Zeiss LSM980 laser scanning confocal microscope at room temperature. Worms were anesthetized with 2 mM levamisole. A region of interest (ROI) was bleached with 30% laser power for 5 ms and the fluorescence intensities in these regions were collected every 5 s and normalized to the initial intensity before bleaching. For analysis, image intensity was measured by the mean and further analyzed by Origin software.

1,6-HD treatment experiments

Adult worms were gently disrupted using a needle to release the germline nuclei. To preserve the integrity and activity of the released nuclei, imaging was promptly performed within a narrow window of 5 min after disruption using a Leica DM4B microscope with a Leica Thunder image-processing system. Dissected gonads were treated with 10% 1,6-HD supplemented with 0.4× M9 and 100 mM NaN3.

Imaging

Images were collected using a Leica DM4B microscope with a Leica Thunder image-processing system. All worms were imaged at the gravid adult stage unless otherwise specified.

Fluorescence intensity quantification

Images of the germline mitotic region of *C. elegans* were captured using a Leica DM4B microscope. The acquired images were processed in ImageJ by adjusting brightness and contrast to enhance piRNA foci visibility. The ROI was manually selected and piRNA foci within the ROI were quantified using the 'analyze particles' tool, with a uniform threshold value set for all images to differentiate foci from background fluorescence. The average fluorescence intensity per piRNA foci was then recorded for statistical analysis.

Recombinant protein expression and purification

The UAD-2 chromodomain (aa 56–129), the UAD-2 IDR (aa 130–519) and the UAD-2 chromodomain + IDR (aa 56–129) were PCR-amplified and cloned and inserted into a plasmid (pET-28a-N8×H-MBP-3C vector) and expressed in *E. coli* BL21(DE3) cells. Protein expression was induced by 0.5 mM IPTG at 16 °C for 24 h. The recombinant proteins were affinity purified through Ni-NTA His-binding resin (GE Healthcare) and the maltose-binding protein tag was cleaved off using PreScission protease. The eluted proteins were further purified using size-exclusion chromatography with a SuperdexTM75 Increase 10/300 GL column or SuperdexTM200 Increase 10/300 GL column (GE Healthcare) on an ÄKTA pure chromatography system.

In vitro UAD-2 droplet formation assay

Purified recombinant proteins were incubated with the fluorochrome Alex488 (Thermo Fisher Scientific) overnight at 4 °C and diluted to varying concentrations in buffer containing 100 mM NaCl, 25 mM NaH_2PO_4, 2 mM EDTA and 5 mM DTT, pH 7.0. Protein solution (6 µl) was loaded onto a glass-bottom confocal dish (Biosharp). The droplet was imaged by a Zeiss LSM 980 confocal microscope with a ×63 oil immersion lens.

ChIP-seq ChIP-seq

ChIP-seq experiments were conducted previously[16,67] and the UAD-2, TOFU-4 and TOFU-5 ChIP-seq data were downloaded from the China National Center for Bioinformation National Genomics Data Center under accession numbers CRA004102 and CRA009179.

Total RNA isolation

Synchronized late young adult worms were washed in M9 and ground with homogenizer lysis buffer (20 mM Tris-HCl pH 7.5, 200 mM NaCl, 2.5 mM $MgCl_2$ and 0.5% Nonidet P-40). The eluates were incubated with TRIzol reagent (Invitrogen) followed by isopropanol precipitation and DNase I digestion (Qiagen).

Decapping total RNA with RppH for piRNA precursor sequencing

Total RNA was treated with FastAP thermosensitive alkaline phosphatase (Thermo Fisher Scientific, EF0651) according to the vendor's protocol. RNA was extracted and precipitated overnight as described for decapping treatment with RppH (New England Biolabs, M0356) according to the vendor's protocol. The resulting RNA was used as input for small RNA library preparation.

RT–qPCR

Synchronized late young adult worms were washed in M9 medium and ground with homogenizer lysis buffer (20 mM Tris-HCl pH 7.5, 200 mM NaCl, 2.5 mM $MgCl_2$ and 0.5% Nonidet P-40). The eluates were incubated with TRIzol reagent (Invitrogen) followed by isopropanol precipitation and DNase I digestion (Qiagen). Complementary DNAs (cDNAs) were generated from RNAs using the HiScript III RT SuperMix for qPCR (Vazyme, R323) according to the vendor's protocol. qPCR was performed using an LightCycler 96 real-time PCR system (Roche) with LightCycler 480 SYBR green I master (Roche, 04707516001). Levels of mRNA of *eft-3* or *ama-1* mRNA were used as controls for sample normalization. The data analysis was performed using a $\Delta\Delta C_t$ approach. The primer sequences are listed in Supplementary Table 2.

Isolation of PRG1-associated RNA

Synchronized late adult GFP::3×FLAG::PRG1 animals were ground by a homogenizer in lysis buffer (20 mM Tris-HCl pH 7.5, 200 mM NaCl, 2.5 mM $MgCl_2$ and 0.5% Nonidet P-40). The lysate was precleared with protein G–agarose beads (Roche) and then incubated with anti-FLAG M2 magnetic beads (Sigma, M8823). The beads were washed extensively and GFP::3×FLAG::PRG1 and associated RNAs were eluted with 100 μg ml^{-1} 3×FLAG peptide (Sigma). The eluates were incubated with TRIzol reagent (Invitrogen), followed by isopropanol precipitation.

Unique molecular index small RNA-seq

Given the large number of piRNA genes and the significant differences in expression levels between different piRNA genes, we chose unique molecular index (UMI) small RNA-seq for a more accurate and reliable quantification of piRNA expression. A total amount of 200 ng of RNA per sample was used as input material for the small RNA library construction. The sequencing libraries were generated using a QIAseq microRNA (miRNA) library kit following the manufacturer's recommendations and index codes were added to attribute sequences to each sample. Briefly, a preadenylated DNA adaptor was ligated to the 3′ ends of miRNA, small interfering RNA (siRNA) and piRNA. After the 3′ ligation reaction, another RNA adaptor was then ligated to the 5′ end. The RT primer containing an integrated UMI subsequently binds to a region of the 3′ adaptor and facilitates conversion of the 3′/5′ ligated miRNAs, siRNA and piRNA into cDNA while assigning a UMI to every small RNA molecule. During RT, a universal sequence is also added that is recognized by the sample indexing primers during library amplification. After RT, the cDNA was cleaned using a streamlined magnetic bead-based method. PCR amplification was performed using the universal forward and reverse primer-containing index. After library amplification, another cleanup of the library was performed using a streamlined magnetic bead-based method. Next, library quality was assessed on the Agilent Bioanalyzer 2100 system using DNA high-sensitivity chips. The clustering of the index-coded samples was performed on a cBot cluster generation system using TruSeq SR cluster kit v3-cBot-HS (Illumina) according to the manufacturer's instructions. After cluster generation, the library preparations were sequenced on an Illumina platform and 150-bp paired-end reads were generated. Raw data were transformed into clean reads by cutting the first 100 bases and removing low-quality reads. Subsequently, clean reads with correct UMI patterns were extracted using UMI tools version 1.0.0, serving as the basis for all downstream analyses to ensure high quality. Lastly, the extracted reads were mapped to the reference sequence with Bowtie and deduplicated using UMI tools on the basis of the mapping coordinates and the attached UMI.

Small RNA-seq

Small RNAs were subjected to deep sequencing using an Illumina platform (Novogene Bioinformatics Technology). Briefly, small RNAs ranging from 18 to 30 nt were gel-purified and ligated to a 3′ adaptor (5′-pUCGUAUGCCGUCUUCUGCUUGidT-3′; p, phosphate; idT, inverted deoxythymidine) and a 5′ adaptor (5′-GUU CAG AGU UCU ACA GUC CGA CGA UC-3′). The ligation products were gel-purified, reverse-transcribed and amplified using Illumina's small RNA primer set (5′-CAA GCA GAA GAC GGC ATA CGA-3′; 5′-AAT GAT ACG GCG ACC ACC GA-3′). The samples were then sequenced using an Illumina Hiseq platform.

RNA-seq analysis

The Illumina-generated raw reads were first filtered to remove adaptors, low-quality tags and contaminants to obtain clean reads at Novogene. For piRNA analysis, clean reads ranging from 17 to 35 nt were mapped to the *C. elegans* transcriptome assembly WS243 using Bowtie2 with default parameters. The numbers of reads targeting each transcript were counted using custom Perl scripts. piRNAs were counted using custom Python scripts dependent on the piRNA annotation from Supplementary Table 3. The number of total reads mapped to the transcriptome minus the number of total reads corresponding to sense ribosomal RNA (rRNA) transcripts (5S, 5.8S, 18S and 26S) was used as the normalization number to exclude the possible degradation fragments of sense rRNAs.

piRNA gene annotations

piRNA annotations and genomic coordinates of piRNA genes were obtained by SAMtools against the *C. elegans* ce10 genome assembly. Information on piRNA clusters and piRNA Ruby motif scores was obtained from previous publications[11,52].

Statistics

Bar graphs with error bars are presented as the mean and s.d. and described in the figure legends. All of the experiments were conducted with independent *C. elegans* animals for the indicated times and described in the figure legends. The details of box plots are described in the figure legends. Statistical analysis is described in the figure legends.

Reporting summary

Further information on research design is available in the Nature Portfolio Reporting Summary linked to this article.

Data availability

The raw sequence data reported in this paper were deposited to the Genome Sequence Archive in National Genomics Data Center, China National Center for Bioinformation and Beijing Institute of Genomics, CAS under accession numbers CRA012796 and CRA018177. Source data are provided with this paper.

References

64. Chen, X. et al. Targeted chromosomal rearrangements via combinatorial use of CRISPR/Cas9 and Cre/LoxP technologies in *Caenorhabditis elegans*. *G3 (Bethesda)* **8**, 2697–2707 (2018).
65. Zhou, X. et al. RdRP-synthesized antisense ribosomal siRNAs silence pre-rRNA via the nuclear RNAi pathway. *Nat. Struct. Mol. Biol.* **24**, 258–269 (2017).
66. Timmons, L., Court, D. L. & Fire, A. Ingestion of bacterially expressed dsRNAs can produce specific and potent genetic interference in *Caenorhabditis elegans*. *Gene* **263**, 103–112 (2001).

67. Hou, X. et al. Systematic characterization of chromodomain proteins reveals an H3K9me1/2 reader regulating aging in *C. elegans*. *Nat. Commun.* **14**, 1254 (2023).

Acknowledgements

We are grateful to the members of the S.G. lab for their comments. We are grateful to the International *C. elegans* Gene Knockout Consortium and the National Bioresource Project for providing the strains. Some strains were provided by the *Caenorhabditis* Genetics Center, which is funded by the National Institutes of Health Office of Research Infrastructure Programs (P40 OD010440). This work was supported by grants from the National Natural Science Foundation of China (32230016 to S.G., 32270583 to C.Z., 32070619 to X.F., 2023M733425 and 32300438 to X.H. and 32090044 and 31971128 to S.X.) and the National Key R&D Program of China (2022YFA1302700 to S.G. and 2019YFA0508403 to S.X.). This work was supported by the Research Funds of Center for Advanced Interdisciplinary Science and Biomedicine of IHM (QYPY20230021 to S.G.). This study was supported in part by the Fundamental Research Funds for the Central Universities. This work was also supported by the Strategic Priority Research Program of the Chinese Academy of Sciences (CAS; XDB 37040202 to S.X.) and the CAS Project for Young Scientists in Basic Research (YSBR-068 to S.X.).

Author contributions

S.X., X. Huang, X.F. and S.G. conceptualized the research. C.Z., X. Huang, X.F. and S.G. designed the research. C.Z., X.S., P.X., Y.T., Q.J., K.R., Y.Z., G.S., D.X., X.C. and X. Huang performed the research. C.W., M.X., Q.Y. and J.C. contributed new reagents. C.Z., X. Hou and J.G. contributed analytic tools and performed the bioinformatics analysis. C.Z., X.F. and S.G. wrote the paper.

Competing interests

The authors declare no competing interests.

Additional information

Extended data is available for this paper at https://doi.org/10.1038/s41594-025-01533-5.

Supplementary information The online version contains supplementary material available at https://doi.org/10.1038/s41594-025-01533-5.

Correspondence and requests for materials should be addressed to Shengqi Xiang, Xinya Huang, Xuezhu Feng or Shouhong Guang.

Peer review information *Nature Structural & Molecular Biology* thanks Wen Tang and the other, anonymous, reviewer(s) for their contribution to the peer review of this work. Peer reviewer reports are available. Primary Handling Editor: Sara Osman, in collaboration with the *Nature Structural & Molecular Biology* team.

Reprints and permissions information is available at www.nature.com/reprints.

https://doi.org/10.1038/s41594-025-01533-5

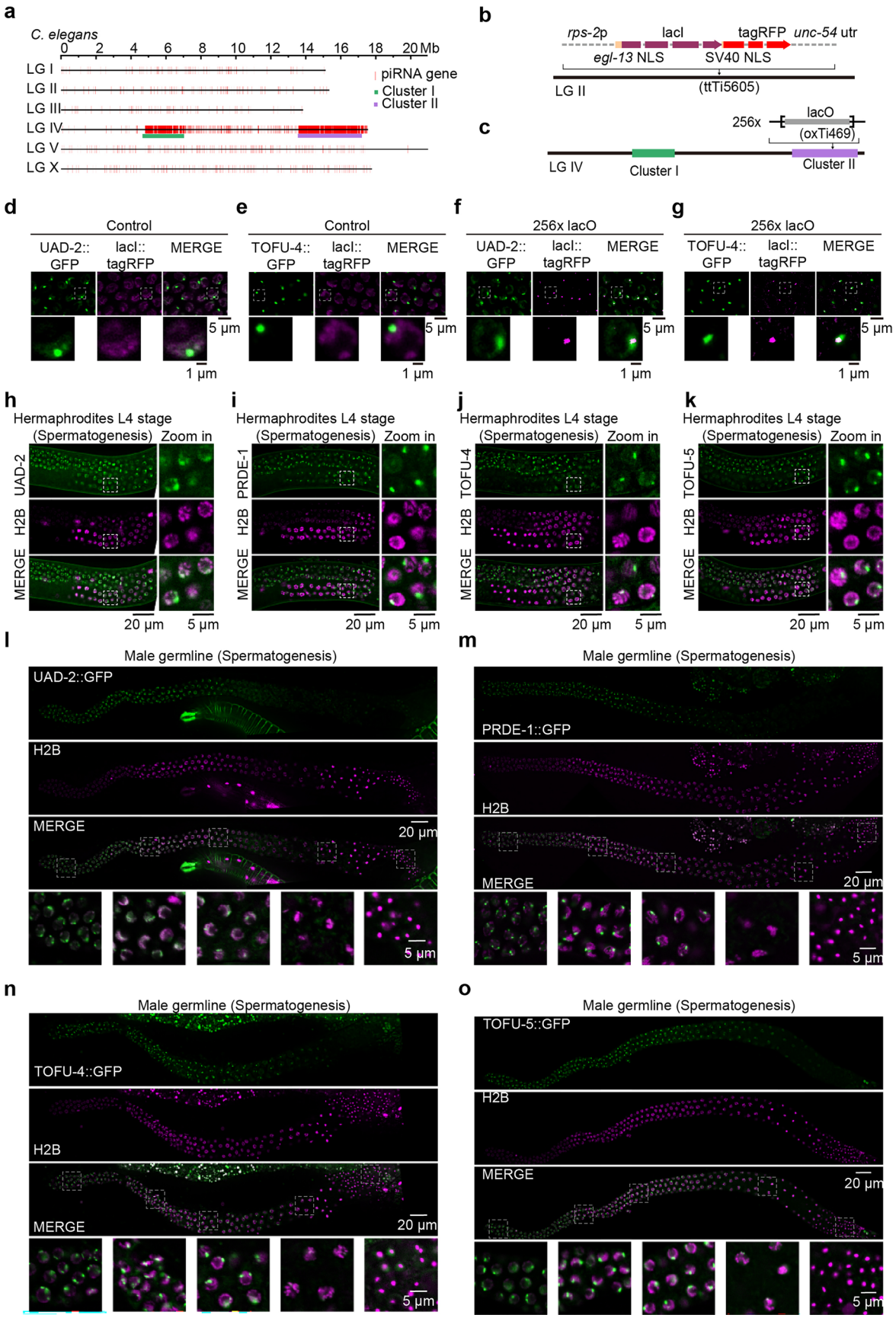

Extended Data Fig. 1 | See next page for caption.

https://doi.org/10.1038/s41594-025-01533-5

Extended Data Fig. 1 | UAD-2 and USTC form distinct foci corresponding to piRNA Cluster II during spermatogenesis in hermaphrodites and males. **a**, Genome-wide distribution of piRNA genes (n = 15365) in *C. elegans*. **b**, Diagram illustrating LacI::tagRFP driven by the *rps-2* promoter and *unc-54* UTR inserted at the LG IV ttti5605 site. **c**. Diagram illustrating 256x LacO inserted into piRNA cluster II (LG IV position: 15,809,942, contributed by the Christian Frøkjær-Jensen lab). **d**. Images showing the subcellular localization of UAD-2::GFP and LacI::tagRFP in the nuclei of pachytene germ cells from wild-type animals. All images were taken by the Leica THUNDER imaging System and deconvoluted using Leica Application Suite X software (version 3.7.4.23463). All images are representative of more than three animals (see also in Extended Data Fig. 1e-o). **e**. Images showing the subcellular localization of TOFU-4::GFP and LacI::tagRFP in the nuclei of pachytene germ cells from wild-type animals. **f**. Images showing the subcellular localization of UAD-2::GFP and LacI::tagRFP in the nuclei of pachytene germ cells from animals with 256xLacO insertions. **g**. Images showing the subcellular localization of TOFU-4::GFP and LacI::tagRFP in the nuclei of pachytene germ cells from animals with 256xLacO insertions. **h-k**. Images displaying the subcellular localization of UAD-2 and USTC components alongside the chromatin marker mCherry::H2B in the spermiogenesis region of the germline in L4 stage hermaphrodite animals. **l-o**. Images displaying the subcellular localization of UAD-2 and USTC components alongside the chromatin marker mCherry::H2B of the germline in adult male animals.

https://doi.org/10.1038/s41594-025-01533-5

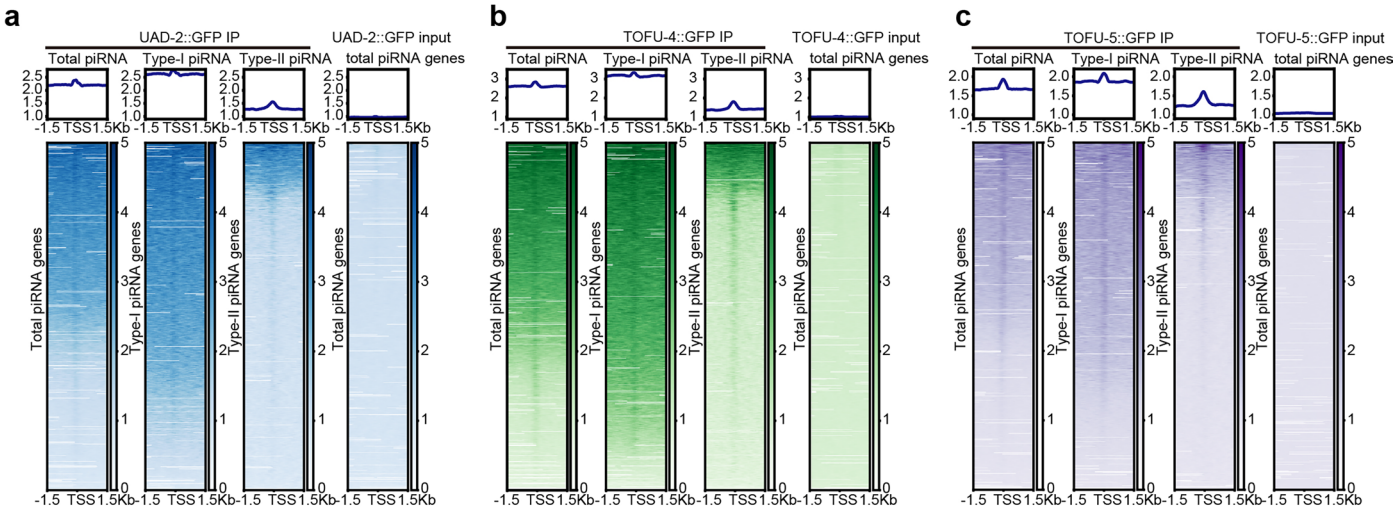

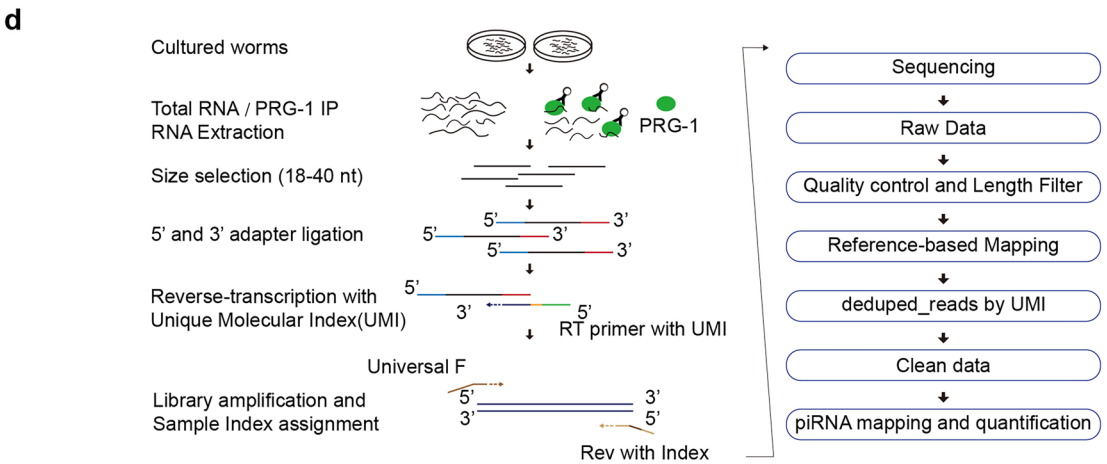

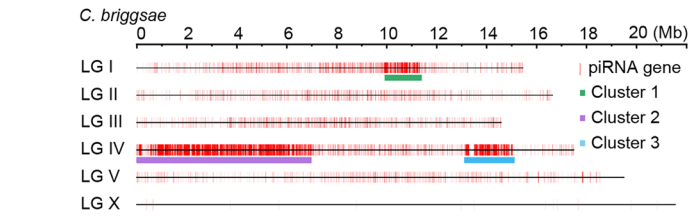

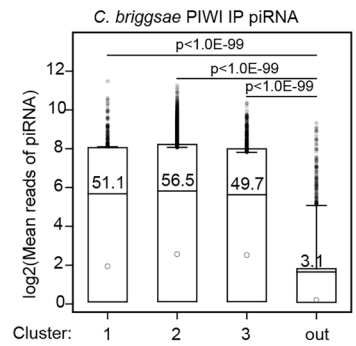

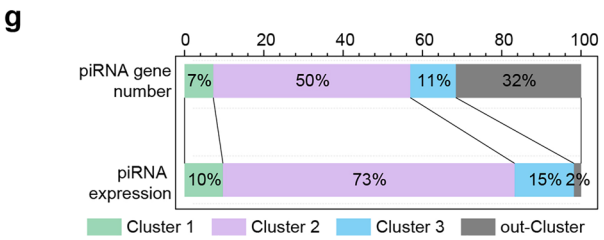

Extended Data Fig. 2 | ChIP-seq profiles of UAD-2 and USTC in *C. elegans*; piRNA gene localization correlates with expression in *C. briggsae*. **a**. Heatmap of ChIP-seq binding profiles of UAD-2 around type I and type II piRNA transcription start sites (TSSs). **b**. Heatmap of ChIP-seq binding profiles of TOFU-4 around type I and type II piRNA transcription start sites (TSSs). **c**. Heatmap of ChIP-seq binding profiles of TOFU-5 around type I and type II piRNA transcription start sites (TSSs). **d**, A flowchart for UMI piRNA sequencing. **e**, Genome-wide distribution of piRNA genes (n = 25883) in *C. briggsae*. **f**, Boxplots presenting $\log_2$(mean of piRNA reads from two biological replicates) for Cbr-PRG-1-associated piRNAs across Cluster 1, Cluster 2, Cluster 3, and out-Cluster in *C. briggsae*. The box itself represented the interquartile range between 5% and 95%, thereby encompassing the middle 90% of the data set. The central horizontal line and the adjacent numeric value within the box represent the mean value. The star within the box represents the median value. Error bars represent the mean ± 1.5 standard deviations (SD), indicating the variability of the data around the mean. Outliers are individually marked as points, representing data points that fall outside the range of mean±1.5 SD. Statistical significance was determined using a two-sample t test. **g**, Graphs presenting the fractional distribution of piRNA genes and their corresponding expression reads (normalized as reads per million from two biological replicates) across Cluster 1, Cluster 2, Cluster 3, and out-Cluster in *C. briggsae*. Source data are provided as a Source Data file.

https://doi.org/10.1038/s41594-025-01533-5

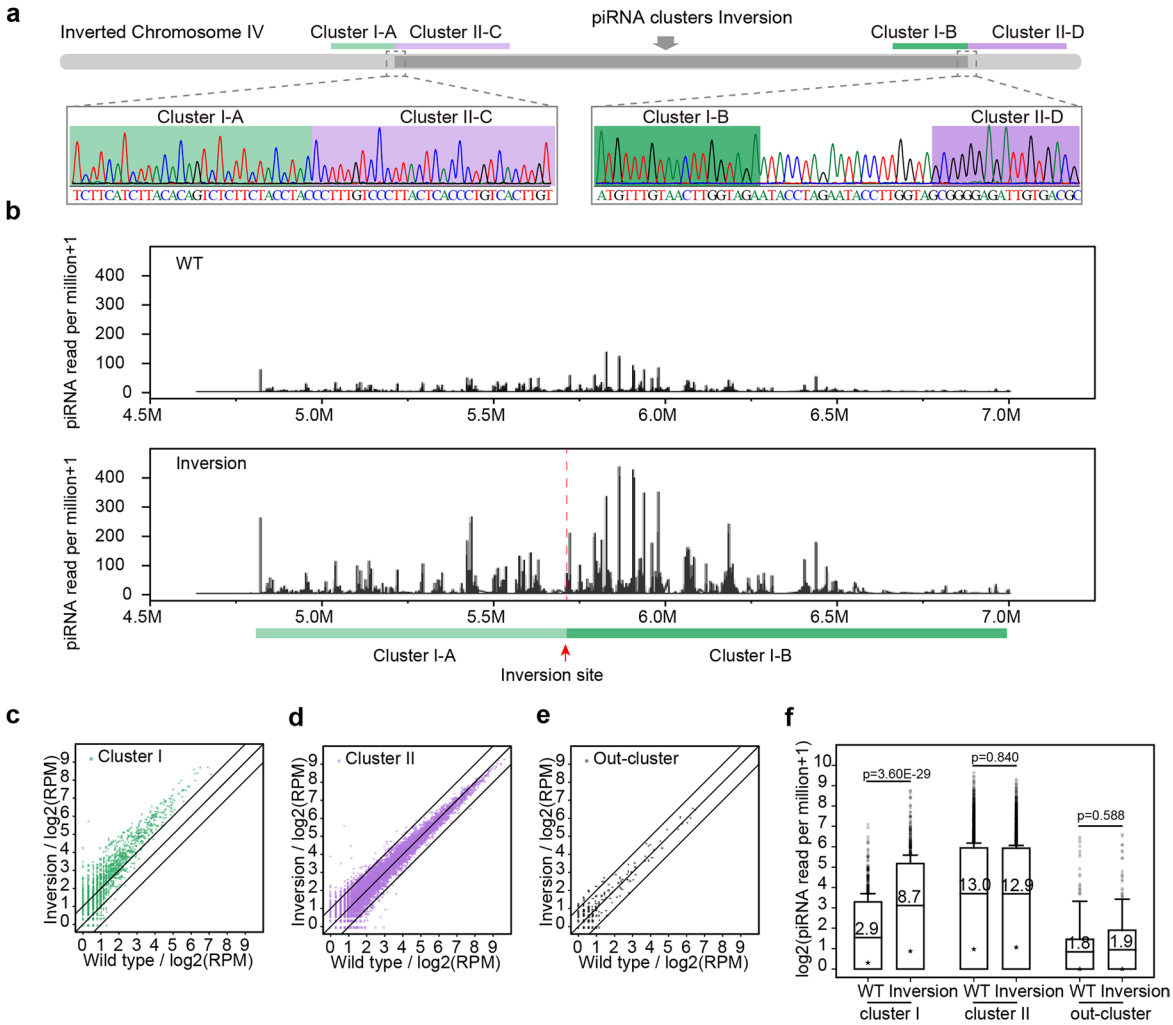

Extended Data Fig. 3 | CRISPR/Cas9-mediated chromosome inversion and translocation alter piRNA expression. a, Diagram showing sequence details of intrachromosomal inversion in LG IV. **b**, Graphs presenting the expression levels of total piRNAs from Cluster I of the indicated animals, based on average reads from two biological replicates, normalized as reads per million+1. **c-e**, Scatter plots displaying the expression levels of Cluster I, Cluster II, and out-Cluster piRNAs in the wild-type (x-axis) and inversion strain (y-axis), based on the $\log_2$(average piRNA reads of two biological replicates), normalized as reads per million+1. **f**, Boxplot revealing $\log_2$(average piRNA reads of two biological replicates) for both the wild-type and inversion strains across Cluster I, Cluster II, and out-Cluster loci. Normalized as reads per million+1. The box itself represented the interquartile range between 5% and 95%, thereby encompassing the middle 90% of the data set. The central horizontal line and the adjacent numeric value within the box represent the mean value. The star within the box represents the median value. Error bars represent the mean ±1.5 standard deviations (SD), indicating the variability of the data around the mean. Outliers are individually marked as points, representing data points that fall outside the range of mean±1.5 SD. Statistical significance was determined using a paired-sample t test.

https://doi.org/10.1038/s41594-025-01533-5

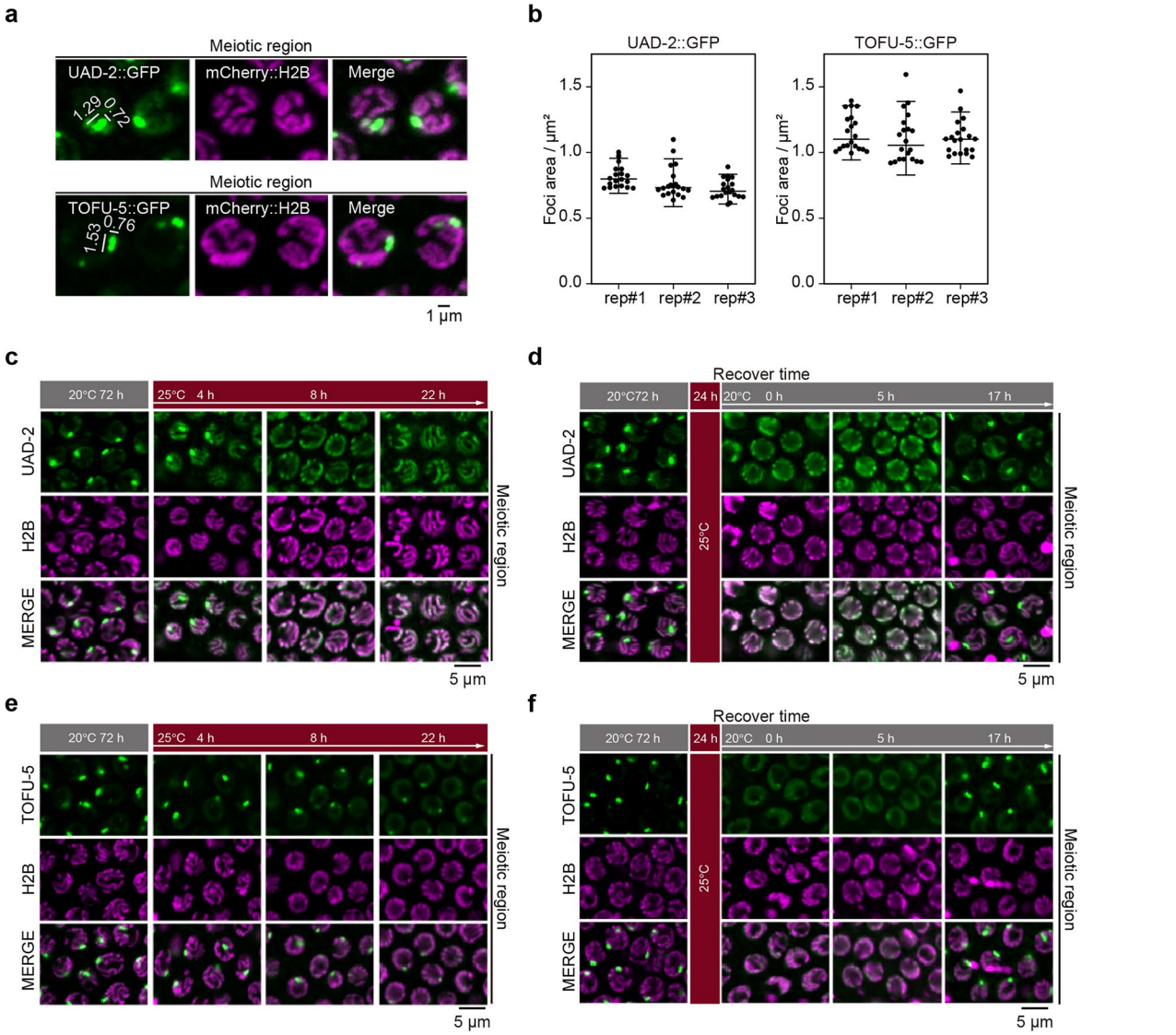

Extended Data Fig. 4 | UAD-2 and the USTC complex form liquid droplet-like condensates at piRNA cluster loci. a, The upper panel shows the localization of UAD-2::GFP and mCherry::H2B in pachytene cells. The lower panel shows the localization of TOFU-5::GFP and mCherry::H2B in pachytene cells. All images were taken by the Leica THUNDER imaging System and deconvoluted using Leica Application Suite X software (version 3.7.4.23463). All images are representative of more than three animals (see also in Extended Data Fig. 4c-f). **b**, Statistical analysis of the focus area for UAD-2::GFP and TOFU-5::GFP in pachytene cells. Quantification of size data from n = 3 independent animals, error bars represent the mean ± 1.5 standard deviations (SD), indicating the variability of the data around the mean. Source data are provided as a Source Data file. **c-f**, The images reflect the subcellular localization of the mentioned proteins in pachytene cells under the indicated culture conditions.

https://doi.org/10.1038/s41594-025-01533-5

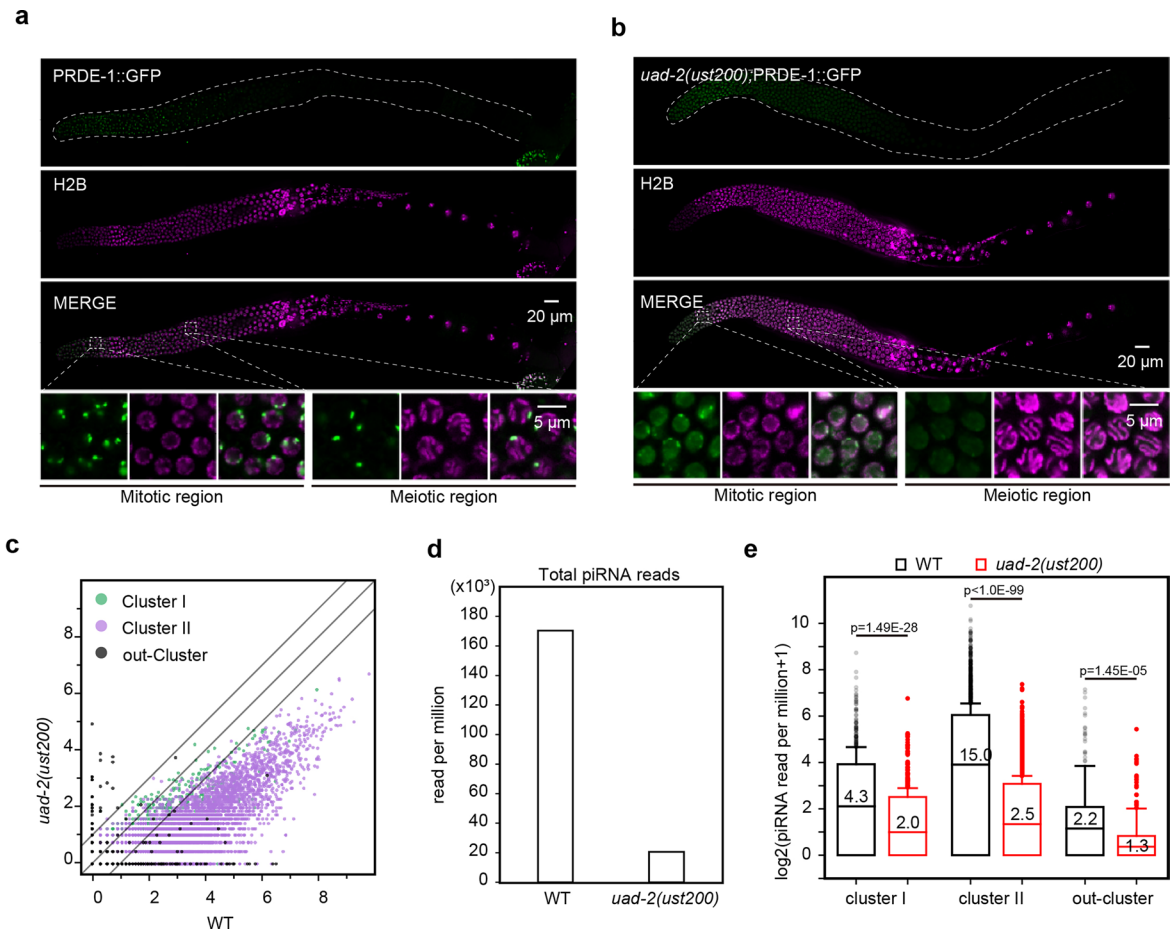

Extended Data Fig. 5 | UAD-2 is required for PDRE-1 foci formation and piRNA expression. a and **b**. Images displaying the subcellular localization of PRDE-1::GFP and the chromatin marker mCherry::H2B in the germline from wild-type animals and *uad-2(ust200)* mutants. **c**. Scatter plots displaying the expression levels of Cluster I, Cluster II, and out-Cluster piRNAs in the wild type (x-axis) and *uad-2(ust200)* mutants (y-axis), based on the $\log_2$(reads per million+1) from a single biological replicate. **d**. Boxplots revealing total piRNA reads per million of the indicated adult animals from a single biological replicate. **e**. Boxplots revealing $\log_2$(piRNA reads per million+1) of the indicated adult animals form a single biological replicate. The box itself represented the interquartile range between 5% and 95%, thereby encompassing the middle 90% of the data set. The central horizontal line and the adjacent numeric value within the box represent the mean value. Error bars represent the mean ± 1.5 standard deviations (SD), indicating the variability of the data around the mean. Outliers are individually marked as points, representing data points that fall outside the range of mean±1.5 SD. Statistical significance was determined using a paired-sample t test.

https://doi.org/10.1038/s41594-025-01533-5

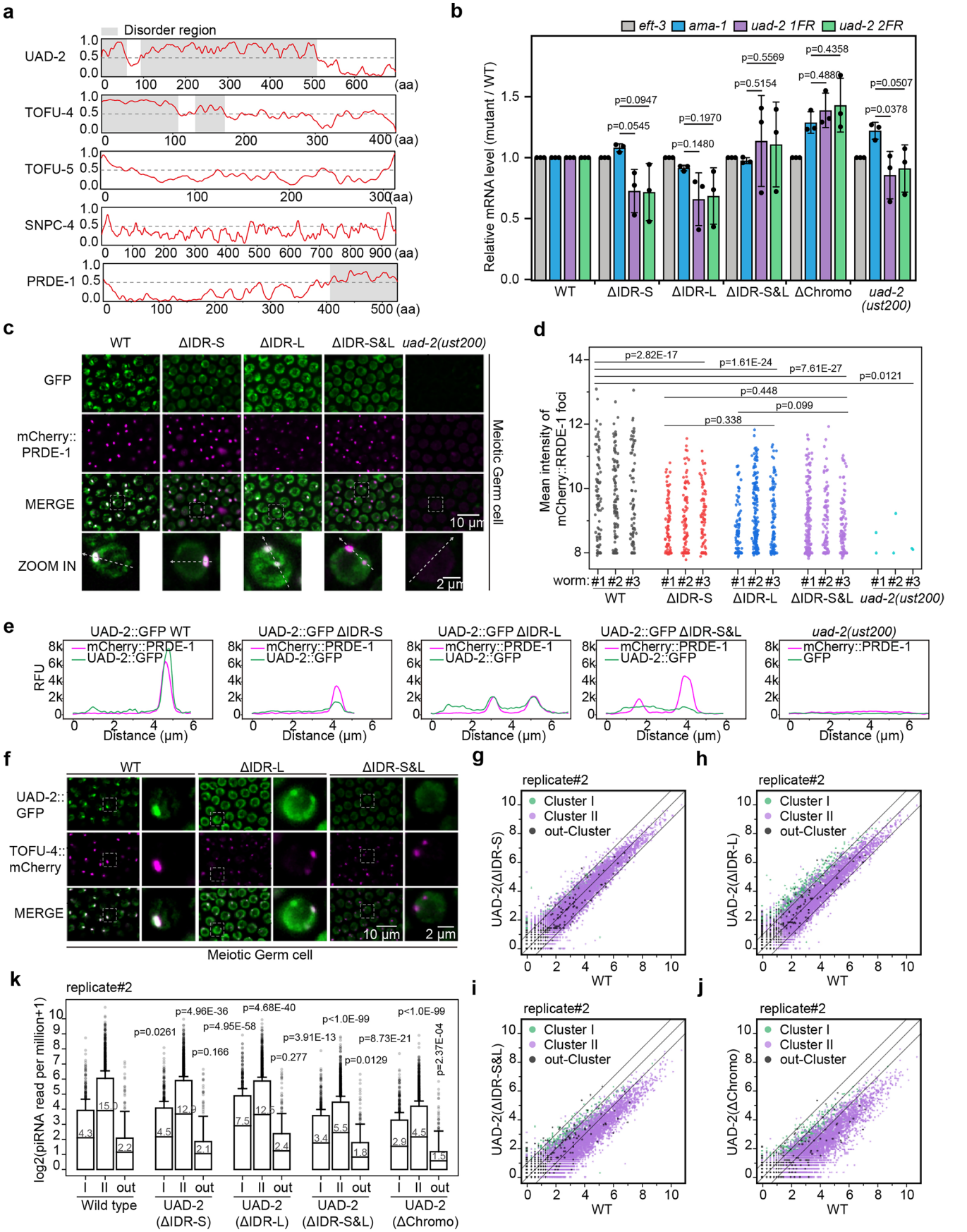

Extended Data Fig. 6 | See next page for caption.

https://doi.org/10.1038/s41594-025-01533-5

Extended Data Fig. 6 | Predicted UAD-2 IDRs are important for PRDE-1 foci formation and piRNA expression. a, IUPred2 prediction of UAD-2 and the USTC components using the IUPred2 long disorder option. **b**, qRT-PCR analysis of UAD-2 mRNA in wild-type animals and *uad-2* deletion mutants. The levels were normalized to *eft-3*. Quantification of qRT-PCR data from n = 3 independent animals, presented as Mean ± SD. Statistical significance was determined using a paired-sample t test. Source data are provided as a Source Data file. **c**. Images showing the subcellular localization of the indicated UAD-2::GFP variants and mCherry::PRDE-1 in pachytene cells. All images were taken by the Leica THUNDER imaging System and deconvoluted using Leica Application Suite X software (version 3.7.4.23463). All images are representative of more than three animals (see also in Extended Data Fig. 6f). **d**, Graphs presenting the relative fluorescence unit intensity (RFU) of mCherry::PRDE-1 for wild-type animals and the indicated UAD-2 variants. The fluorescence intensity threshold is set to 8–255. Three worms were analyzed for each strain. Statistical significance was determined using a two-sample t test. Source data are provided as a Source Data file. **e**. Graphs presenting the relative fluorescence unit intensity (RFU) of wild-type animals and the indicated UAD-2 variants, marked by the dashed line. **f**. Images showing the subcellular localization of the indicated UAD-2::GFP variants and TOFU-4:mCherry in pachytene cells. **g-j**. Scatter plots displaying the second biological replicate expression levels of Cluster I, Cluster II, and out-Cluster piRNAs in the wild-type (x-axis) and indicated mutants (y-axis), based on the $\log_2$(reads per million+1). **k**. Boxplots revealing $\log_2$(piRNA reads per million+1) of the indicated adult animals of the second biological replicate. The box itself represented the interquartile range between 5% and 95%, thereby encompassing the middle 90% of the data set. The central horizontal line and the adjacent numeric value within the box represent the mean value. Error bars represent the mean ± 1.5 standard deviations (SD), indicating the variability of the data around the mean. Outliers are individually marked as points, representing data points that fall outside the range of mean±1.5 SD. Statistical significance was determined using a paired-sample t test.

https://doi.org/10.1038/s41594-025-01533-5

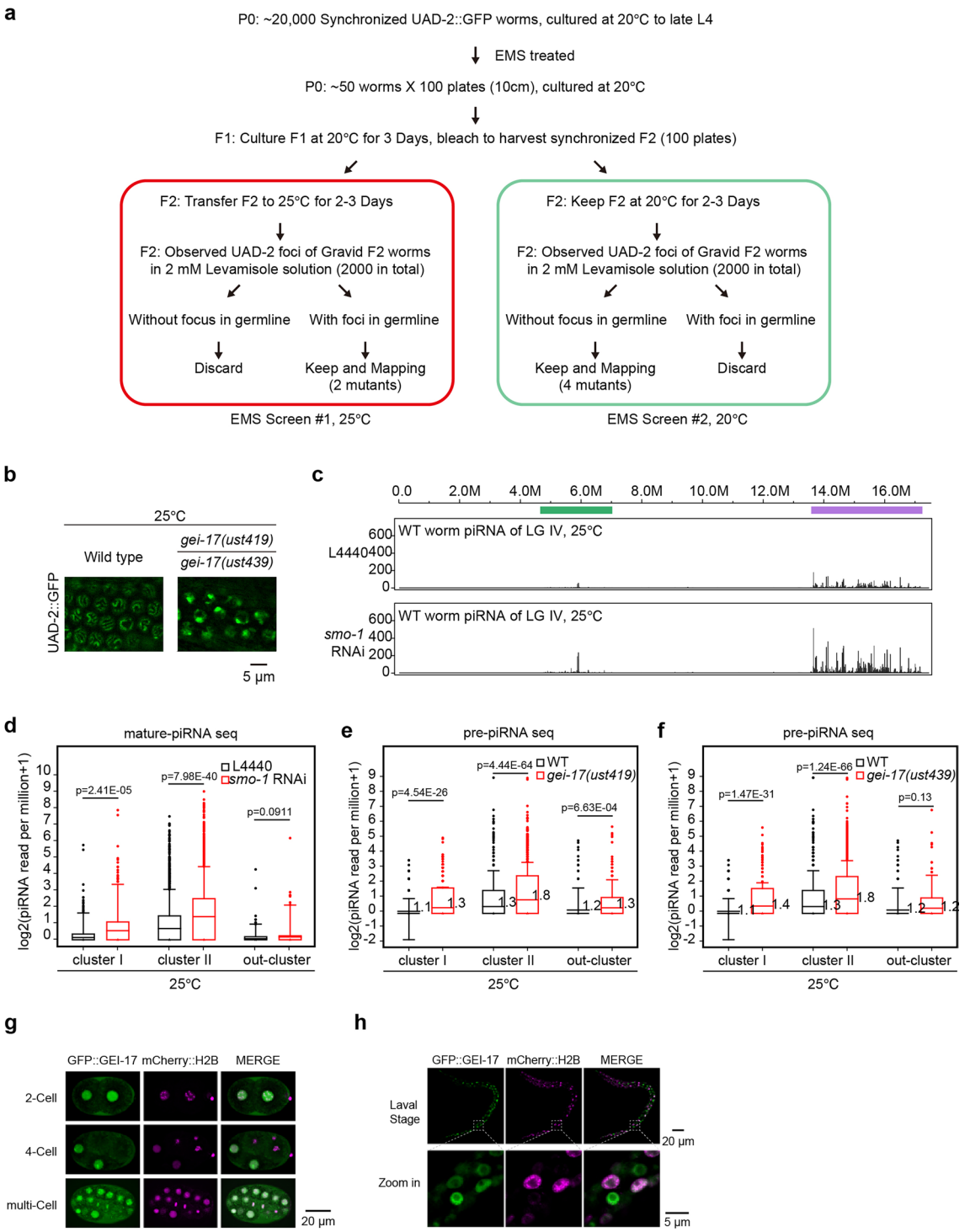

Extended Data Fig. 7 | Forward genetic screening identifies factors suppressing UAD-2 foci formation. a, Forward genetic screening procedures for UAD-2::GFP regulators at 20 °C and 25 °C. **b**, Complementation test for two alleles of *gei-17* at 25 °C. All images were taken by the Leica THUNDER imaging System and deconvoluted using Leica Application Suite X software (version 3.7.4.23463). All images are representative of more than three animals (see also in Extended Data Fig. 7g and h). **c**, Expression levels of total piRNAs from LG IV in WT worms fed L4440 and *smo-1* dsRNA at 25 °C, normalized as reads per million+1. **d**, Boxplots illustrating $\log_2$(piRNA reads per million+1) for WT worms fed with L4440 and *smo-1* dsRNA at 25 °C from a single biological replicate. The box itself represented the interquartile range between 5% and 95%, thereby encompassing the middle 90% of the data set. The central horizontal line and the adjacent numeric value within the box represent the mean value. Error bars represent the mean ±1.5 standard deviations (SD), indicating the variability of the data around the mean. Outliers are individually marked as points, representing data points that fall outside the range of mean±1.5 SD (see also in Extended Data Fig. 7e and f). Statistical significance was determined using a paired-sample t test. **e** and **f**, Boxplots illustrating $\log_2$(pre-piRNA reads per million+1) for WT worms and *gei-17* mutants at 25 °C. Statistical significance was determined using a paired-sample t test. **g** and **h**, Images displaying GFP::FLAG::Degron::GEI-17 (green) and mCherry::H2B (magenta) in embryos and larval animals.

https://doi.org/10.1038/s41594-025-01533-5

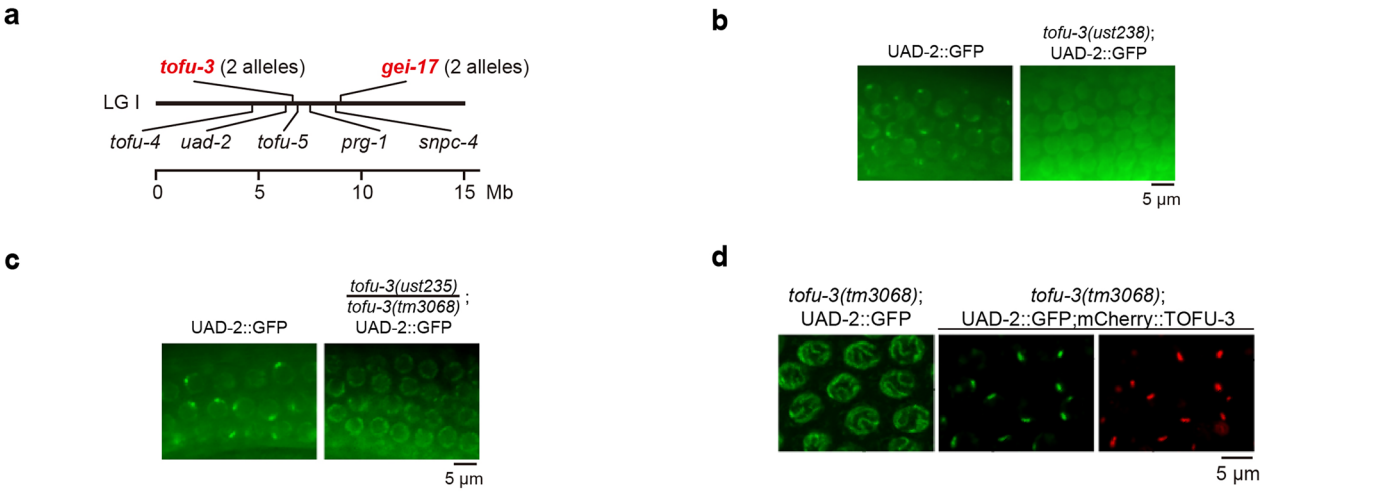

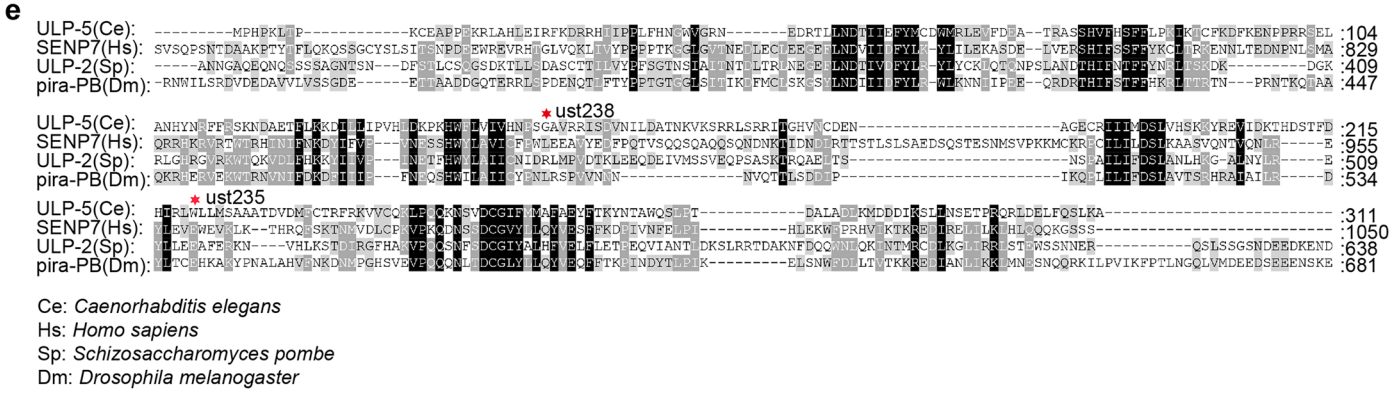

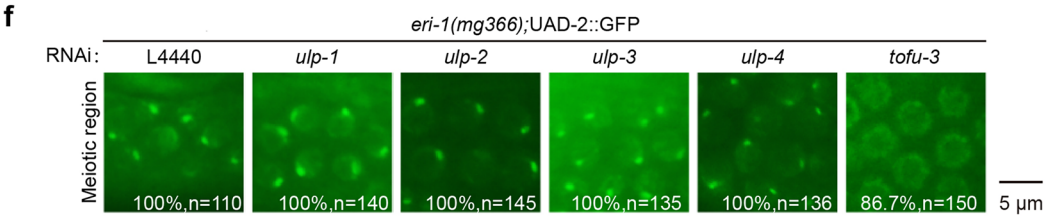

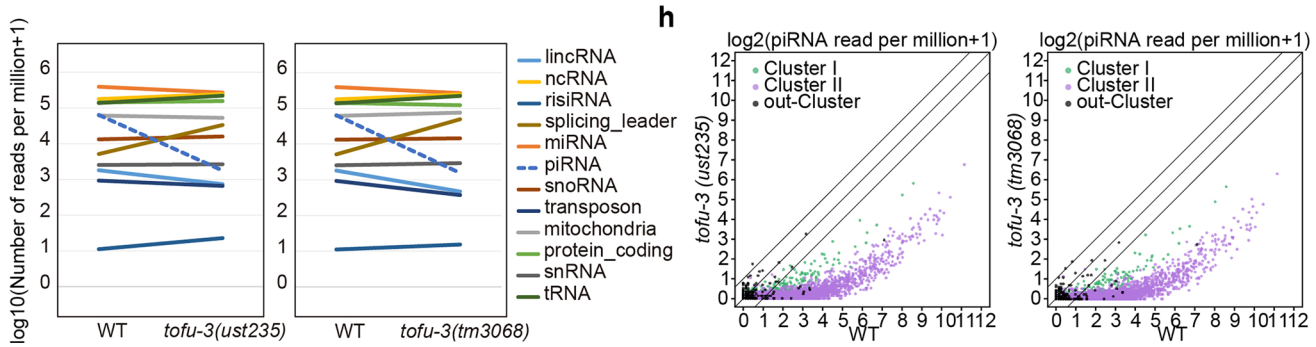

Extended Data Fig. 8 | Forward genetic screening identified TOFU-3 as required for UAD-2 condensate formation and piRNA production. **a**. Schematic representation summarizing piRNA genes and alleles identified from the two forward genetic screens. **b**. Images of the meiotic region of the indicated adult animal germline grown at 20 °C. All images were taken by the Leica THUNDER imaging System and deconvoluted using Leica Application Suite X software (version 3.7.4.23463). All images are representative of more than three animals (see also in Extended Data Fig. 8c, d and f). **c**, Complementation test of two alleles of *tofu-3* at 20 °C. **d**, Images of pachytene cells of the indicated adult animals grown at 20 °C. mCherry::TOFU-3 rescued UAD-2::GFP foci formation in *tofu-3(tm3068)* cells. **e**, Sequence alignment of the TOFU-3 (ULP-5) protein. **f**, Subcellular localization of UAD-2::GFP in pachytene cells in *eri-1(mg366)*;UAD-2::GFP worms fed the indicated RNAi bacteria. n, the number of independent animals tested. Source data are provided as a Source Data file. **g**, Deep sequencing of total small RNAs of the indicated adult animals from one biological replicate. Blue dashed lines indicate piRNAs. **h**, Scatter plots depicting the expression levels of Cluster I, Cluster II, and out-Cluster piRNAs in the wild-type (x-axis) and *tofu-3* mutant strains (y-axis) from one biological replicate, normalized as reads per million+1.

https://doi.org/10.1038/s41594-025-01533-5

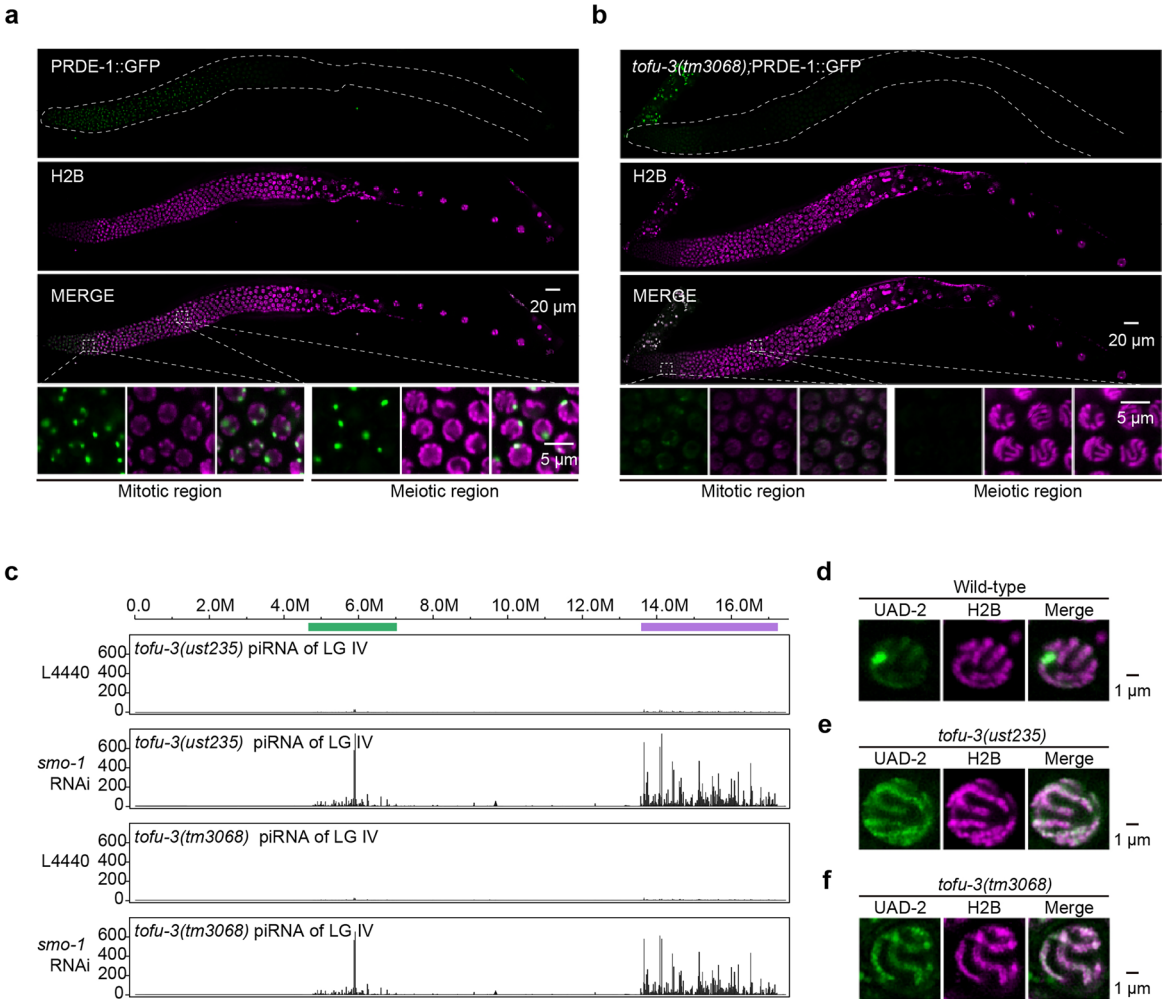

Extended Data Fig. 9 | UAD-2 is required for PDRE-1 foci formation and piRNA expression. a and **b**. Images displaying the subcellular localization of PRDE-1::GFP and the chromatin marker mCherry::H2B in the germline from wild-type animals and *tofu-3(tm3068)* mutants. All images were taken by the Leica THUNDER imaging System and deconvoluted using Leica Application Suite X software (version 3.7.4.23463). All images are representative of more than three animals (see also in Extended Data Fig. 9d–f). **c**, Expression levels of total piRNAs from LG IV of the indicated adult animals cultured at 20 °C, normalized as reads per million+1 from one biological replicate. **d-f**, Subcellular localization of UAD-2::GFP and mCherry::H2B in pachytene cells from WT, *tofu-3(ust235)* and t*ofu-3(tm3068)* mutant worms.

https://doi.org/10.1038/s41594-025-01533-5

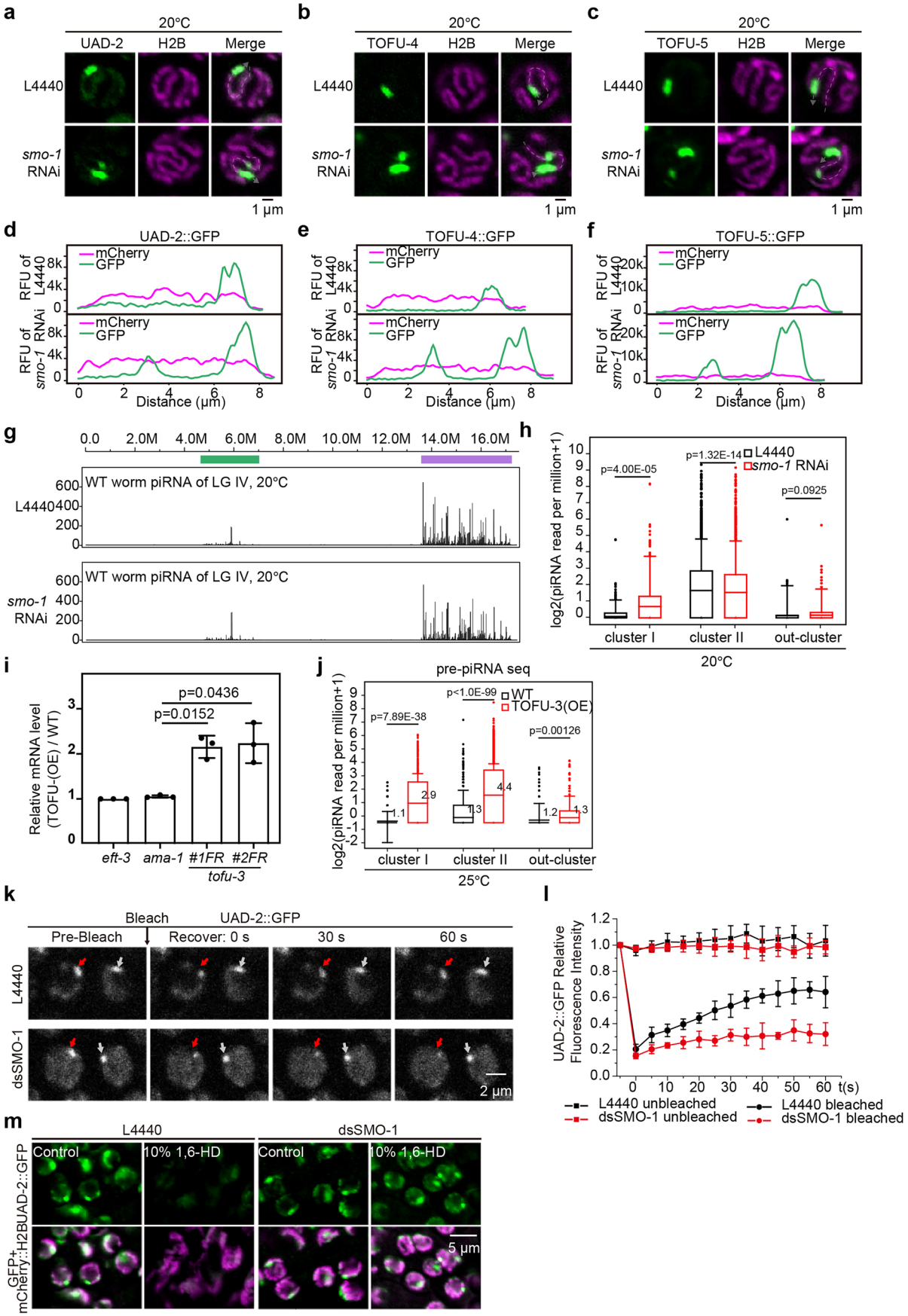

Extended Data Fig. 10 | See next page for caption.

https://doi.org/10.1038/s41594-025-01533-5

Extended Data Fig. 10 | SMO-1 suppresses piRNA expression and increases UAD-2 mobility. a-c, Subcellular localization of UAD-2::GFP, TOFU-4::GFP and TOFU-5::GFP with mCherry::H2B in pachytene cells of WT worms fed L4440 and *smo-1* dsRNA at 20 °C. All images were taken by the Leica THUNDER imaging System and deconvoluted using Leica Application Suite X software (version 3.7.4.23463). All images are representative of more than three animals (see also in Extended Data Fig. 10m). **d-f**, Relative fluorescence unit intensity (RFU) indicated by dashed lines along chromosome IV of (a-c). Source data are provided as a Source Data file. **g**, Expression levels of total piRNAs from LG IV in specified adult animals grown at 20 °C, normalized as reads per million+1. **h**, Boxplots illustrating $\log_2$(piRNA reads per million+1) for the indicated adult animals from one biological replicate. The box itself represented the interquartile range between 5% and 95%, thereby encompassing the middle 90% of the data set. The central horizontal line within the box represents the mean value. Error bars represent the mean ± 1.5 standard deviations (SD), indicating the variability of the data around the mean. Outliers are individually marked as points, representing data points that fall outside the range of mean±1.5 SD (see also in Extended Data Fig. 10j). Statistical significance was determined using a paired-sample t test. **i**, qRT-PCR analysis of *tofu-3* mRNA in wild-type animals and mCherry::TOFU-3 animals. The levels were normalized to *eft-3*. Quantification of qRT-PCR data from n = 3 independent animals, error bars represent the mean ± 1.5 standard deviations (SD), indicating the variability of the data around the mean. Statistical significance was determined using a paired-sample t test. Source data are provided as a Source Data file. **j**. Boxplots illustrating $\log_2$(pre-piRNA reads per million+1) for wild-type worms and mCherry::TOFU-3 animals at 25 °C from one biological replicate. Statistical significance was determined using a paired-sample t test. **k**, Fluorescence recovery after photobleaching (FRAP) of UAD-2::GFP under L4440 and *smo-1* RNAi was conducted using a Zeiss LSM980 confocal microscope. All images are representative of 6 animals. **l**, Graphs presenting the relative fluorescence unit intensity (RFU) of the control area and bleached area of UAD-2 under L4440 and *smo-1* RNAi. Quantification of FRAP data from n = 6 independent animals, error bars represent the mean ± 1.5 standard deviations (SD), indicating the variability of the data around the mean. Source data are provided as a Source Data file. **m**, Images showing germline nuclei expressing UAD-2::GFP. After release by needle disruption, the germline was imaged within 5 minutes using a Leica Thunder imaging system. Germlines were treated with 10% 1,6-hexanediol to prohibit phase separation.

nature portfolio

Corresponding author(s): Shouhong Guang

Last updated by author(s): Jan 14, 2025

Reporting Summary

Nature Portfolio wishes to improve the reproducibility of the work that we publish. This form provides structure for consistency and transparency in reporting. For further information on Nature Portfolio policies, see our Editorial Policies and the Editorial Policy Checklist.

Statistics

For all statistical analyses, confirm that the following items are present in the figure legend, table legend, main text, or Methods section.

n/a	Confirmed	
☐	☒	The exact sample size (*n*) for each experimental group/condition, given as a discrete number and unit of measurement
☐	☒	A statement on whether measurements were taken from distinct samples or whether the same sample was measured repeatedly
☐	☒	The statistical test(s) used AND whether they are one- or two-sided *Only common tests should be described solely by name; describe more complex techniques in the Methods section.*
☒	☐	A description of all covariates tested
☒	☐	A description of any assumptions or corrections, such as tests of normality and adjustment for multiple comparisons
☐	☒	A full description of the statistical parameters including central tendency (e.g. means) or other basic estimates (e.g. regression coefficient) AND variation (e.g. standard deviation) or associated estimates of uncertainty (e.g. confidence intervals)
☐	☒	For null hypothesis testing, the test statistic (e.g. *F*, *t*, *r*) with confidence intervals, effect sizes, degrees of freedom and *P* value noted *Give P values as exact values whenever suitable.*
☒	☐	For Bayesian analysis, information on the choice of priors and Markov chain Monte Carlo settings
☒	☐	For hierarchical and complex designs, identification of the appropriate level for tests and full reporting of outcomes
☒	☐	Estimates of effect sizes (e.g. Cohen's *d*, Pearson's *r*), indicating how they were calculated

Our web collection on statistics for biologists contains articles on many of the points above.

Software and code

Policy information about availability of computer code

Data collection	Leica LAS Microscope Software (version X) were used to acquire images.
Data analysis	small RNA-seq was performed by Bowtie2 with default parameters. Quantification of Relative fluorescence unit intensity (RFU) by Leica LAS Microscope Software (version X) image process system.

For manuscripts utilizing custom algorithms or software that are central to the research but not yet described in published literature, software must be made available to editors and reviewers. We strongly encourage code deposition in a community repository (e.g. GitHub). See the Nature Portfolio guidelines for submitting code & software for further information.

Data

Policy information about availability of data

All manuscripts must include a data availability statement. This statement should provide the following information, where applicable:

- Accession codes, unique identifiers, or web links for publicly available datasets
- A description of any restrictions on data availability
- For clinical datasets or third party data, please ensure that the statement adheres to our policy

Data Availability: The raw sequence data reported in this paper have been deposited in the Genome Sequence Archive in National Genomics Data Center, China National Center for Bioinformation / Beijing Institute of Genomics, Chinese Academy of Sciences (GSA: CRA012796) and are publicly accessible at https://ngdc.cncb.ac.cn/gsa.

Research involving human participants, their data, or biological material

Policy information about studies with human participants or human data. See also policy information about sex, gender (identity/presentation), and sexual orientation and race, ethnicity and racism.

Reporting on sex and gender	No human research participants were involved.
Reporting on race, ethnicity, or other socially relevant groupings	No human research participants were involved.
Population characteristics	No human research participants were involved.
Recruitment	No human research participants were involved.
Ethics oversight	No human research participants were involved.

Note that full information on the approval of the study protocol must also be provided in the manuscript.

Field-specific reporting

Please select the one below that is the best fit for your research. If you are not sure, read the appropriate sections before making your selection.

☒ Life sciences ☐ Behavioural & social sciences ☐ Ecological, evolutionary & environmental sciences

For a reference copy of the document with all sections, see nature.com/documents/nr-reporting-summary-flat.pdf

Life sciences study design

All studies must disclose on these points even when the disclosure is negative.

Sample size	For experiments involving imaging and quantification, numbers of animals were > =3.
Data exclusions	No data were excluded from the analysis.
Replication	Phenotype experiments were repeated at least 3 times. All attempts of replication were successful.
Randomization	Animals used in the experiments were cultured simultaneously on the same plates and selected randomly to control or experimental groups.
Blinding	The investigators were blinded to group allocation during data collection and analysis.

Reporting for specific materials, systems and methods

We require information from authors about some types of materials, experimental systems and methods used in many studies. Here, indicate whether each material, system or method listed is relevant to your study. If you are not sure if a list item applies to your research, read the appropriate section before selecting a response.

Materials & experimental systems

n/a	Involved in the study
☐	☒ Antibodies
☒	☐ Eukaryotic cell lines
☒	☐ Palaeontology and archaeology
☐	☒ Animals and other organisms
☒	☐ Clinical data
☒	☐ Dual use research of concern
☒	☐ Plants

Methods

n/a	Involved in the study
☒	☐ ChIP-seq
☒	☐ Flow cytometry
☒	☐ MRI-based neuroimaging

Antibodies

Antibodies used	Anti-GFP antibody (abcam ab290, lot # GR3320917-1), used at 1.5:1000
Validation	Anti-GFP antibody (abcam ab290) antibody has been validated by abcam by demonstrating Western blot and Immunocytochemistry (see website). This antibody was also validated in our previous works (Weng et al., 2019 and Huang et al., 2021).

Animals and other research organisms

Policy information about studies involving animals; ARRIVE guidelines recommended for reporting animal research, and Sex and Gender in Research

Laboratory animals	Caenorhabditis elegans. Adult staged animals were used in small RNA-seq and imaging.
Wild animals	No wild animals were used in this study.
Reporting on sex	Hermaphrodite animals were used in this study.
Field-collected samples	No field-collected samples were used in this study.
Ethics oversight	Caenorhabditis elegans was used in this study and no ethical approval was required.

Note that full information on the approval of the study protocol must also be provided in the manuscript.

Plants

Seed stocks	No plant seed stocks were involved in this study.
Novel plant genotypes	No plant was involved in this study.
Authentication	No plant was involved in this study.